

Stellar and Dark Matter Halo Properties of LAEs at $z \sim 2$

Haruka KUSAKABE¹, Kazuhiro SHIMASAKU^{1,2}, Masami OUCHI^{3,4}, Kimihiko NAKAJIMA⁵, Ryosuke GOTO¹, Takuya HASHIMOTO^{1, 6, 7}, Akira KONNO^{1,4}, Yuichi HARIKANE^{4,8}, John D. SILVERMAN³ and Peter L. CAPAK^{9, 10}

¹Department of Astronomy, Graduate School of Science, The University of Tokyo, 7-3-1 Hongo, Bunkyo-ku, Tokyo 113-0033, Japan

²Research Center for the Early Universe, The University of Tokyo, 7-3-1 Hongo, Bunkyo-ku, Tokyo 113-0033, Japan

³Kavli Institute for the Physics and Mathematics of the Universe (Kavli IPMU, WPI), The University of Tokyo, 5-1-5 Kashiwanoha, Kashiwa, Chiba 277-8583, Japan

⁴Institute for Cosmic Ray Research, The University of Tokyo, 5-1-5 Kashiwanoha, Kashiwa, Chiba 277-8582, Japan

⁵European Southern Observatory, Karl-Schwarzschild-Strasse 2, D-85748 Garching, b. München, Germany

⁶College of General Education, Osaka Sangyo University, 3-1-1 Nakagaito, Daito, Osaka 574-8530, Japan

⁷National Astronomical Observatory of Japan, 2-21-1 Osawa, Mitaka, Tokyo 181-8588, Japan

⁸Department of Physics, Graduate School of Science, The University of Tokyo, 7-3-1 Hongo, Bunkyo, Tokyo 113-0033, Japan

⁹California Institute of Technology, MC 105-24, 1200 East California Blvd., Pasadena, CA 91125, USA

¹⁰Infrared Processing and Analysis Center, California Institute of Technology, MC 100-22, 770 South Wilson Ave., Pasadena, CA 91125, USA

*E-mail: kusakabe@astron.s.u-tokyo.ac.jp

Received (reception date); Accepted (acceptation date)

Abstract

We present average stellar population properties and dark matter halo masses of $z \sim 2$ Ly α emitters (LAEs) from SED fitting to stacked images and clustering analysis, respectively, using $\simeq 1250$ $NB387 \leq 25.5$ objects in four separate fields of $\simeq 1$ deg² in total. With an average stellar mass of $10.2 \pm 3.0 \times 10^8 M_{\odot}$ and star formation rate of $3.4 \pm 0.7 M_{\odot} \text{ yr}^{-1}$, the LAEs lie on a low-mass extrapolation of the star-formation main sequence (MS) with moderate star formation. Their effective dark matter halo mass is estimated to be $4.0^{+5.1}_{-2.9} \times 10^{10} M_{\odot}$ with $b_{g, \text{eff}}^{\text{ave}} = 1.22^{+0.16}_{-0.18}$, which is lower than that of $z \sim 2$ LAEs ($b_{g, \text{eff}} = 1.8 \pm 0.3$) obtained by a previous study based on a three times smaller area with a probability of 96%, although this difference can be explained if the cosmic variance in these $b_{g, \text{eff}}$ is taken into account. Such a low halo mass, if it implies a low HI gas mass, is consistent with high Ly α escape fractions of LAEs observed. Despite the low halo mass and being in the MS mode, our LAEs have a relatively high stellar-to-halo mass ratio (SHMR) and baryon conversion efficiency, converting baryons into stars efficiently until the observed time. The extended Press-Schechter formalism predicts that at $z = 0$ our LAEs are typically embedded in halos with masses similar to that of

the Large Magellanic Cloud (LMC); if their SFRs are largely suppressed after $z \sim 2$ as reported for the LMC itself, they will also have similar SHMRs to the LMC.

Key words: galaxies: evolution — galaxies: high-redshift — galaxies: star formation — galaxies: halos

1 Introduction

Galaxies assemble their stellar mass through star formation and galaxy-galaxy merging under the gravitational influence of dark matter halos hosting them, which also grow by mass accretion and merging. Hence, observations of stellar population properties and their halo-mass dependence for galaxies in the past are key to tracing the mass growth history of galaxies and constraining physical processes which control star formation. In this paper we focus on low-mass galaxies, which are “building blocks” of present-day galaxies over a wide mass range.

Nebular emission lines are useful to detect faint (or low-mass) galaxies at high redshift (z), among which $\text{Ly}\alpha$ line has been used most commonly. Tens of thousands of $\text{Ly}\alpha$ emitters (LAEs) have been selected so far by narrowband (NB) imaging observations ($z \sim 2\text{--}7$: e.g., Malhotra & Rhoads 2002; Taniguchi et al. 2005; Shimasaku et al. 2006; Gronwall et al. 2007; Ota et al. 2008; Ouchi et al. 2008; Guaita et al. 2010; Hayes et al. 2010; Hu et al. 2010; Ouchi et al. 2010; Ciardullo et al. 2012; Nakajima et al. 2012; Yamada et al. 2012; Konno 2014; Sandberg et al. 2015; Shimakawa et al. 2017; Shibuya et al. 2017a) and/or spectroscopically identified ($z \sim 0\text{--}7$: e.g., Shapley et al. 2003; Kashikawa et al. 2006; Reddy et al. 2008; Cowie et al. 2010; Blanc et al. 2011; Dressler et al. 2011; Kashikawa et al. 2011; Curtis-Lake et al. 2012; Mallery et al. 2012; Nakajima et al. 2013; Erb et al. 2014; Hayes et al. 2014; Hashimoto et al. 2013; Hathi et al. 2016; Karman et al. 2017; Shibuya et al. 2017b) and they are one of the important populations of high- z star forming galaxies.

Typical LAEs at high redshifts have low stellar masses ($M_\star \lesssim 10^9 M_\odot$: Ono et al. 2010a; Guaita et al. 2011; Kusakabe et al. 2015; Hagen et al. 2016; Shimakawa et al. 2017). They are also dust-poor (Lai et al. 2008; Blanc et al. 2011; Kusakabe et al. 2015), metal-poor (Nakajima et al. 2012, 2013; Nakajima & Ouchi 2014; Kojima et al. 2017), and young star forming galaxies (Gawiser et al. 2007; Hagen et al. 2014), although a small fraction of them are evolved dusty galaxies with high stellar masses (Nilsson et al. 2009; Ono et al. 2010b; Pentericci et al. 2010; Oteo et al. 2012).

Since their dust emission is typically too faint to be detected by current infrared (IR) telescopes without gravitational lensing, SFR values largely vary depending on the method to measure them, making it difficult to determine in which star formation (SF) mode they are between the burst mode and the main-sequence (MS) mode (Finkelstein et al. 2015; Hagen et al. 2016; Hashimoto et al. 2017; Shimakawa et al. 2017). Only at $z \sim 2$

has the SFR of average LAEs been estimated from ultraviolet (UV) and dust emission, by means of stacking, from which they are found to lie on the star formation main sequence (SFMS: e.g., Daddi et al. 2007), although the analysis is limited to only a single survey field (Kusakabe et al. 2015). Recent observations have revealed that stellar properties of LAEs are similar to those of other emission line galaxies (at $z \sim 2$: Hagen et al. 2016). Shimakawa et al. (2017) have also found that LAEs at $M_\star \lesssim 10^{10} M_\odot$ obey the same $M_\star\text{--}SFR$ and $M_\star\text{--size}$ relations as $\text{H}\alpha$ emitters (HAEs) at $z = 2.5$. Thus, there is a possibility that LAEs are normal star-forming galaxies in the low stellar mass regime at high redshift.

With regard to dark matter halos, LAEs have been found to reside in low-mass halos from clustering analysis ($M_h \sim 10^{10}\text{--}10^{12} M_\odot$ over $z \sim 2\text{--}7$: e.g., Ouchi et al. 2005; Kovač et al. 2007; Gawiser et al. 2007; Shioya et al. 2009; Guaita et al. 2010; Ouchi et al. 2010; Bielby et al. 2016; Diener et al. 2017; Ouchi et al. 2017). These results imply that LAEs at $z \sim 4\text{--}7$ and $z \sim 2\text{--}3$ evolve into massive elliptical galaxies and L_\star galaxies at $z = 0$, respectively. In either case, high- z LAEs are good candidates of “building blocks” of mature galaxies in the local Universe (see also Rauch et al. 2008; Dressler et al. 2011) because they are embedded in the lowest-mass halos among all the high- z galaxy populations.

With stellar masses, SFR s, and halo masses in hand, one can obtain stellar to halo mass ratios ($\equiv M_\star/M_h$: $SHMR$) and baryon conversion efficiencies ($\equiv SFR/\text{baryon accretion rate}$: BCE) to quantify the star formation efficiency in dark matter halos. The $SHMR$ measures the time-integrated (time-averaged) efficiency of star formation until the observed time, while the BCE measures the efficiency at the observed time. The SF mode also tells us the nature of star formation in terms of stellar mass growth.

For LAEs, one can probably measure these parameters most reliably at $z \sim 2$, because this redshift is high enough that $\text{Ly}\alpha$ line is redshifted into the optical regime where a wide-field ground-based $\text{Ly}\alpha$ survey, critical for clustering analysis, is possible, and low enough that deep rest-frame near-infrared (NIR) photometry, critical for SED fitting of faint galaxies like LAEs, is still possible with Spitzer/IRAC. This redshift is also scientifically interesting because the star-formation activity in the universe is highest.

There is, however, only one clustering study at $z \sim 2$, by Guaita et al. (2010), obtaining a relatively high halo mass of $\log(M_h/M_\odot) \sim 11.5^{+0.4}_{-0.5}$, which implies an $SHMR$ and BCE

comparable to or lower than those from the average relations by Behroozi et al. (2013) at the same mass. However, this mass estimate may suffer from statistical uncertainties due to a small sample size ($N \sim 250$ objects) and systematic uncertainties from cosmic variance due to a small survey area ($\sim 0.3 \text{ deg}^2$). As for the SF mode, the study using deep IRAC data by Kusakabe et al. (2015) is based on only one field. A larger number of sources from a larger survey area with deep multi-wavelength data are needed to overcome these uncertainties.

In this paper, we study star forming activity and its dependence on halo mass for $z \sim 2$ LAEs using ~ 1250 NB-selected LAEs from four deep survey fields with a total area of $\simeq 1 \text{ deg}^2$. Section 2 summarizes the data and sample used in this study. In section 3 we estimate halo masses from clustering analysis. In section 4 we perform SED fitting to stacked imaging data to measure stellar population parameters. The *SHMR* and *BCE* are calculated and compared with literature results in section 5. Section 6 is devoted to discuss the results obtained in the previous sections. Conclusions are given in Section 7.

Throughout this paper, we adopt a flat cosmological model with the matter density $\Omega_m = 0.3$, the cosmological constant $\Omega_\Lambda = 0.7$, the baryon density $\Omega_b = 0.045$, the Hubble constant $H_0 = 70 \text{ km s}^{-1} \text{ Mpc}^{-1}$ ($h_{100} = 0.7$), the power-law index of the primordial power spectrum $n_s = 1$, and the linear amplitude of mass fluctuations in the universe $\sigma_8 = 0.8$, which are consistent with the latest Planck results (Planck Collaboration 2016). We assume a Salpeter initial mass function (IMF: Salpeter 1955)¹. Magnitudes are given in the AB system (Oke & Gunn 1983) and coordinates are given in J2000. Distances are expressed in comoving units. We use “log” to denote a logarithm with a base 10 (\log_{10}).

2 Data and Sample

2.1 Sample Selection

Our LAE samples are constructed in four deep survey fields, the Subaru/XMM-Newton Deep Survey (SXDS) field (Furusawa et al. 2008), the Cosmic Evolution Survey (COSMOS) field (Scoville et al. 2007), the Hubble Deep Field North (HDFN: Capak et al. 2004), and the Chandra Deep Field South (CDFS: Giacconi et al. 2001). We select LAEs at $z = 2.14\text{--}2.22$ using the narrow band *NB387* (Nakajima et al. 2012) as described in selection papers (Nakajima et al. 2012, 2013; Kusakabe et al. 2015; Konno et al. 2016). The threshold of rest-frame equivalent width, EW_0 , of $\text{Ly}\alpha$ emission is $EW_0(\text{Ly}\alpha) \geq 20\text{--}30\text{\AA}$.

¹ To rescale stellar masses in previous studies assuming a Chabrier or Kroupa IMF (Kroupa 2001; Chabrier & Chabrier 2003), we divide them by a constant factor of 0.61 or 0.66, respectively. Similarly, to convert SFRs in the literature with a Chabrier or Kroupa IMF, we divide them by a constant factor of 0.63 or 0.67, respectively.

Table 1. Details of the data.

field (arcmin ²) /band	PSF ('')	aperture diameter ('')	aperture correction (mag)
SXDS (~ 1240)			
<i>NB387</i>	0.88	2.0	0.17
<i>B</i>	0.84	2.0	0.17
<i>V</i>	0.8	2.0	0.15
<i>R</i>	0.82	2.0	0.16
<i>i'</i>	0.8	2.0	0.16
<i>z'</i>	0.81	2.0	0.16
<i>J</i>	0.85	2.0	0.15
<i>H</i>	0.85	2.0	0.15
<i>K</i>	0.85	2.0	0.16
IRAC ch1	1.7	3.0	0.52
IRAC ch2	1.7	3.0	0.55
COSMOS (~ 740)			
<i>NB387</i>	0.95	2.0	0.25
<i>B</i>	0.95	2.0	0.12
<i>V</i>	1.32	2.0	0.33
<i>r'</i>	1.04	2.0	0.19
<i>i'</i>	0.95	2.0	0.12
<i>z'</i>	1.14	2.0	0.25
<i>J</i>	0.79	2.0	0.3
<i>H</i>	0.76	2.0	0.2
<i>Ks</i>	0.75	2.0	0.2
IRAC ch1	1.7	3.0	0.52
IRAC ch2	1.7	3.0	0.55
HDFN (~ 780)			
<i>NB387</i>	0.89	2.0	0.14
<i>B</i>	0.77	2.0	0.15
<i>V</i>	1.24	2.0	0.20
<i>R</i>	1.18	2.0	0.22
<i>I</i>	0.80	2.0	0.13
<i>z'</i>	0.81	2.0	0.15
<i>J</i>	0.84	2.0	0.17
<i>H</i>	0.84	2.0	0.17
<i>Ks</i>	0.84	2.0	0.18
IRAC ch1	1.7	3.0	0.52
IRAC ch2	1.7	3.0	0.55
CDFS (~ 580)			
<i>NB387</i>	0.85	2.0	0.13
<i>B</i>	1.0	2.0	0.20
<i>V</i>	0.94	2.0	0.18
<i>R</i>	0.83	2.0	0.16
<i>I</i>	0.95	2.0	0.22
<i>z'</i>	1.1	2.0	0.24
<i>J</i>	0.80	2.0	0.22
<i>H</i>	1.5	2.0	0.55
<i>Ks</i>	0.70	2.0	0.18
IRAC ch1	1.7	3.0	0.52
IRAC ch2	1.7	3.0	0.55

Note. The FWHM of PSF, aperture diameter, and aperture correction are shown. The value in parentheses shows the area used in clustering analysis.

In this paper, we do not use LAEs in SXDS-E and SXDS-W because of the shallowness of the data. For each field we also remove LAEs in regions with short net exposure times due to dithering for accurate clustering analysis. In the SXDS field (SXDS-C, N, and S), we use overlapped regions of the images to examine if there exists an offset in the $NB387$ zero point. A non-negligible offset of 0.06 mag is found in SXDS-N and is corrected. In the other three fields, we examine the $NB387$ zero point using colors of Galactic stars calculated from Gunn & Stryker (1983) and apply 0.1 mag correction to CDFS. Note that such an amount of correction changes $\text{Ly}\alpha$ luminosities only slightly. Our entire sample consists of 2441 LAEs from $\simeq 1$ square degree (each survey area size is shown in table 1). Note that 1937 LAEs with $NB387_{\text{tot}} \leq 26.3$ are used in clustering analysis and 1248 LAEs with $NB387_{\text{tot}} \leq 25.5$ are used to calculate the average value of effective biases (see figure 1 and table 2).

2.2 Contamination Fraction

Possible interlopers in our LAE samples are categorized into (i) active galactic nuclei (AGNs), (ii) low- z line emitters with an emission line misclassified as $\text{Ly}\alpha$, and (iii) continuum sources selected as LAEs owing to photometric errors in the selection bands. Sources detected in either X-ray, UV, or radio are regarded as AGNs and have been removed as described in the selection papers. Candidate low- z emitters are [O II] $\lambda 3727$ emitters at $z \simeq 0.04$, Mg II $\lambda 2798$ emitters at $z \simeq 0.4$, and C IV $\lambda 1550$ and C III] $\lambda 1909$ emitters at $z \simeq 1.5$. However, the survey volume of [O II] emitters at $z \simeq 0.04$ is three orders of magnitude smaller than that of LAEs at $z = 2.2$. Moreover, the $EW_0([\text{O II}])$ of the vast majority of [O II] emitters is too small to meet our color selection ($\geq 70 \text{ \AA}$) (see Konno et al. 2016). Mg II, C IV and C III] emitters should have large equivalent widths ($EW_0 \geq 30 \text{ \AA}$) but they are likely to be AGNs and hence have been removed.

We evaluate the contamination fraction by sources which do not satisfy the selection criteria (hereafter, unselected sources) for each field using Monte Carlo simulations. Assuming that the relative distribution of unselected sources in the two-color selection plane is unchanged with $NB387$ magnitude, we use bright ($NB387 \leq 24$ mag where photometric errors are negligible in all three selection bands) unselected sources to create a mock catalog by adding photometric errors, where the distribution of $NB387$ magnitudes of simulated sources is set equal to that of real objects.

We then apply the same selection as for the real catalog to obtain the number of objects passing the selection. The contamination fraction is calculated by dividing this number by the number of LAEs actually selected. We find that the contamination fraction at $NB387 \leq 25.5$ mag is 10–20% for all four fields. This contamination fraction is conservative in the sense

that real LAEs with $EW_0(\text{Ly}\alpha)$ below the selection threshold ($EW_0(\text{Ly}\alpha) \geq 20\text{--}30 \text{ \AA}$) are used to create the mock catalogs.

Spectroscopic follow-up observations of $\text{Ly}\alpha$ emission of bright LAEs in our sample ($NB387 \leq 24.5$ mag) have also been carried out with Magellan/IMACS, MagE, and Keck/LRIS by Nakajima et al. (2012), Hashimoto et al. (2013), Shibuya et al. (2014), Hashimoto et al. (2015), Hashimoto et al. (2017), and M. Rauch et al. (2017, in preparation). In total, more than 40 LAEs are spectroscopically confirmed and no foreground interlopers such as [O II] emitters at $z = 0.04$ are found (Nakajima et al. 2012). Although faint LAEs cannot be confirmed spectroscopically, the contamination fraction is probably not high. Indeed, Konno et al. (2016) have not applied contamination correction in deriving luminosity functions. On the basis of the results of the Monte Carlo simulations and the spectroscopic follow-up observations, 0–20%, we conservatively adopt $10 \pm 10\%$ for the contamination fraction. This value is similar to a previous result for NB-selected LAEs at $z \sim 2$ ($7 \pm 7\%$; Guaita et al. 2010). The effect of contamination sources is taken into account in clustering analysis (see section 3.2). On the other hand, it is negligible in SED fitting for median-stacked subsamples in section 4.

2.3 Imaging Data for SED Fitting

We use ten broadband images for SED fitting: five optical bands – B, V, R (or r), i (or i') and z (or z'); three NIR bands – J, H and K (or K_s); and two mid-infrared (MIR) bands – IRAC ch1 and ch2. The PSFs of the images are matched in each field (not in each sub-field). The aperture corrections for MIR images converting $3''$ aperture magnitudes to total magnitudes are taken from Ono et al. (2010a, see table 1). For each field, a K-band or NIR detected catalog is used to clean IRAC photometry in section 4.1. Here we summarize the data used in SED fitting and IRAC cleaning in the four fields.

SXDS fields The images used for SED fitting are: B, V, R, i' , and z' images with Subaru/Suprime-Cam from the Subaru/XMM-Newton Deep Survey project (Furusawa et al. 2008, SXDS); J, H , and K images from the data release 8 of the UKIRT/WFCAM UKIDSS/UDS project (Lawrence et al. 2007, Almaini et al. in prep.); Spitzer/IRAC 3.6 μm (ch1) and 4.5 μm (ch2) images from the Spitzer Large Area Survey with Hyper-Suprime-Cam (SPLASH) project (SPLASH: PI: P. Capak; Laigle et al. 2016). All images are publicly available except the SPLASH data. The aperture corrections for optical and NIR images are given in Nakajima et al. (2013). The catalog used to clean IRAC photometry is constructed from the K -band image of the UKIDSS/UDS data release 11 (Almaini et al. in prep).

COSMOS field We use the publicly available B, V, r', i' , and

z' images with Subaru/Suprime-Cam by the Cosmic Evolution Survey (COSMOS: Capak et al. 2007; Taniguchi et al. 2007) and J , H , and K_s images with the VISTA/VIRCAM from the first data release of the UltraVISTA survey (McCracken et al. 2012). We also use Spitzer/IRAC ch1 and ch2 images from the SPLASH project. The aperture corrections for the optical images are derived in Nakajima et al. (2013) and those for the NIR images follow McCracken et al. (2012). The catalog used to clean IRAC photometry is from Laigle et al. (2016), for which sources have been detected in the z' YJKs images.

HDFN field The images used for SED fitting are: B , V , R , I , and z' images with Subaru/Suprime-Cam from the Hubble Deep Field North Survey (HDFN: Capak et al. 2004); J (Lin et al. 2012), H (Hsu et al. 2017 in prep.), and K_s (Wang et al. 2010) images with CFHT/WIRCam; Spitzer/IRAC ch1 and ch2 images from the Spitzer Extended Deep Survey (SEDS: Ashby et al. 2013). We use reduced J -band and K_s -band images given in Lin et al. (2012). All images are publicly available. The aperture corrections for the optical images are given in Nakajima et al. (2013). Those of the NIR images with a $2''$ radius aperture are evaluated using bright and isolated point sources in each band. We measure fluxes for 20 bright point sources in a series of apertures from $2''$ with an interval of $0.''1$ and find that the fluxes level off for $> 7.''8$ apertures. We measure the difference in magnitude between the $2''$ and $7.''8$ apertures of 100 bright and isolated sources and perform Gaussian fitting to the histogram of differences. We adopt the best-fit mean as the aperture correction term. The catalog used to clean IRAC photometry is constructed from the K -band image (Wang et al. 2010).

CDFS fields We use the publicly available B , V , R , and I images with the MPG 2.2m telescope/WFI by the Garching-Bonn Deep Survey (GaBoDS: Hildebrandt et al. 2006; Cardamone et al. 2010), the z' image with the CTIO 4m Blanco telescope/Mosaic-II camera from the Multiwavelength Survey by Yale-Chile (MUSYC: Taylor et al. 2009; Cardamone et al. 2010), the H image with the ESO-NTT telescope/SofI camera by the MUSYC (Moy et al. 2003; Cardamone et al. 2010), and the J and K_s images by the Taiwan ECDFS Near-Infrared Survey (TENIS: Hsieh et al. 2012). We also use the Spitzer/IRAC ch1 and ch2 images from the Spitzer IRAC/MUSYC Public Legacy Survey in the Extended CDF-South (SIMPLE: Damen et al. 2011). The aperture corrections for optical and NIR photometry are derived in a similar manner to those in HDFN. The catalog used to clean IRAC photometry is from Hsieh et al. (2012),

Table 2. The definition of subsamples and the number of objects in each subsample.

field	$NB387_{\text{tot}}$ magnitude limit (mag)				
	25.0	25.3	25.5	25.8	26.3
SXDS	161	368	601 (93)	-	-
COSMOS	119	205	297 (21)	526	-
HDFN	119	200	299 (56)	588	-
CDFS	27	41	51 (4)	92	222

Note. The value in parentheses shows the number of objects used for SED fitting.

for which sources have been detected in the J image.

The FWHM of the PSF, aperture diameters, and aperture corrections are summarized in table 1.

3 Clustering Analysis

3.1 Subsamples Divided by $NB387$ Magnitude

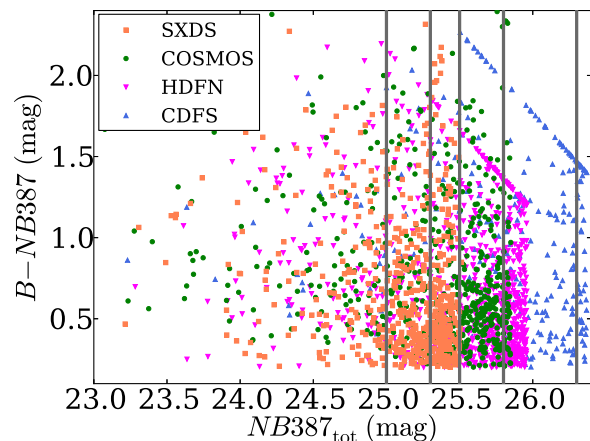


Fig. 1. $B - NB387$ ($NB387$ excess) plotted against $NB387$ total magnitude. Orange, green, magenta, and blue points show LAEs in SXDS, COSMOS, HDFN, and CDFS, respectively. LAEs are divided into cumulative subsamples with different limiting magnitudes shown by gray solid lines: $NB387_{\text{tot}} \leq 25.0$ mag, 25.3 mag, 25.5 mag, 25.8 mag, and 26.3 mag. (Color online)

The distribution of $B - NB387$ as a function of total $NB387$ magnitude, $NB387_{\text{tot}}$, is shown in figure 1. In order to examine the dependence of halo mass on the total $NB387$ magnitude, we divide our LAE sample of each field into up to five cumulative subsamples with different limiting magnitudes, as shown in table 2 and figure 1. 1937 LAEs with $NB387_{\text{tot}} \leq 25.5$ are used in the clustering analysis.

3.2 Angular Correlation Function

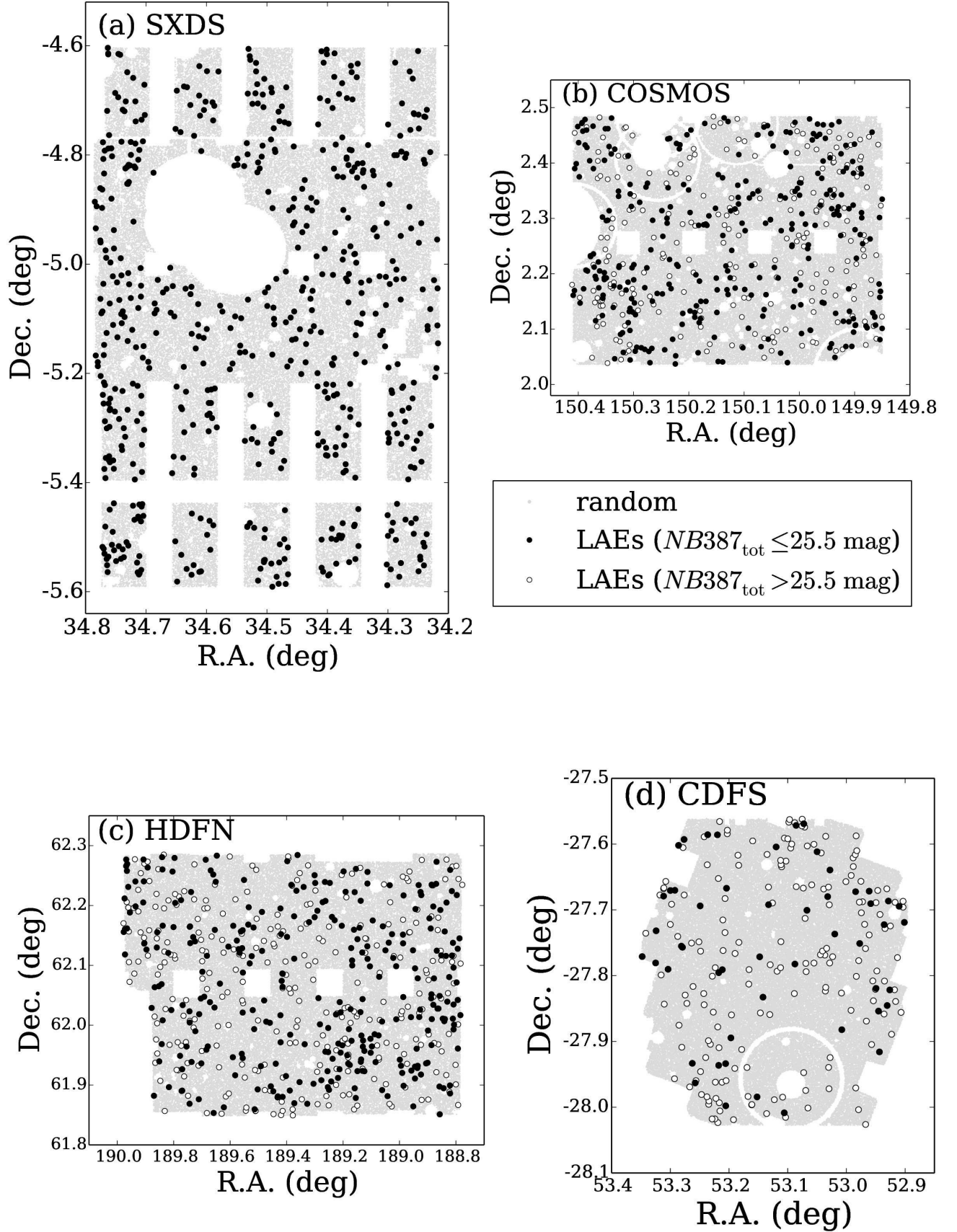


Fig. 2. Sky distribution of LAEs in SXDS (panel [a]), COSMOS ([b]), HDFN ([c]), and CDFS ([d]). Filled and open black circles represent objects with $NB_{\text{tot}} \leq 25.5$ mag and $NB_{\text{tot}} > 25.5$ mag, respectively. Shown in white are masked regions.

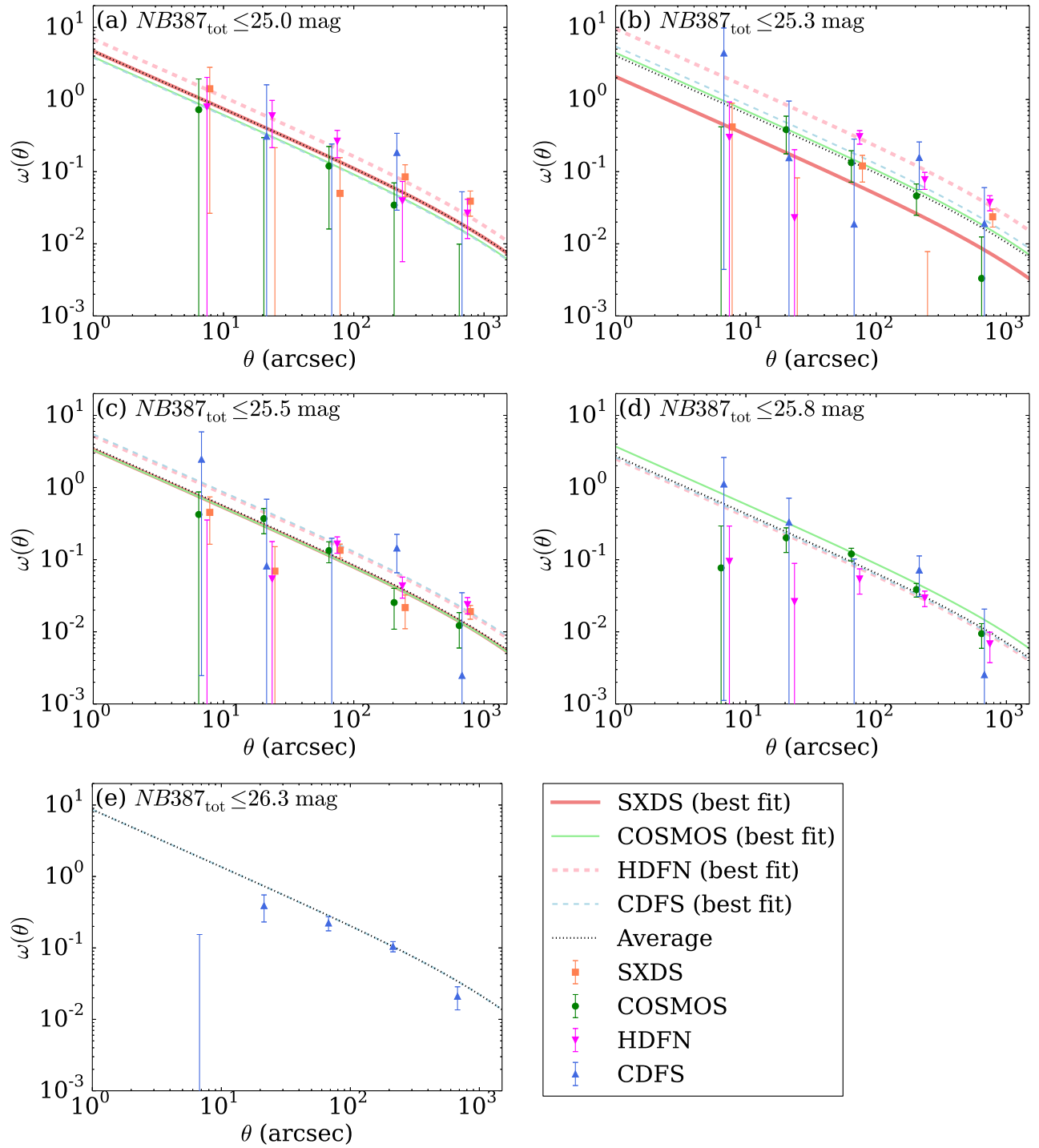


Fig. 3. ACF measurements for LAEs with $NB387_{\text{tot}} \leq 25.0$ (panel [a]), $NB387_{\text{tot}} \leq 25.3$ ([b]), $NB387_{\text{tot}} \leq 25.5$ ([c]), $NB387_{\text{tot}} \leq 25.8$ ([d]), and $NB387_{\text{tot}} \leq 26.3$ ([e]). For each panel, orange, green, magenta, and blue circles represent measurements in SXDS, COSMOS, HDFN, and CDFS, respectively. Solid thick light coral, solid thin light green, dashed thick light pink, and dashed thin light blue lines indicate the best-fit ACFs with fixed $\beta = 0.8$ in SXDS, COSMOS, HDFN, and CDFS, respectively. A solid dotted black line shows the average of the best-fit ACFs over the four fields. (Color online)

Dark matter halo masses of our LAEs are derived from clustering analysis. The sky distributions of the LAEs in the four fields are shown in figure 2². We measure the angular two-point correlation function (ACF), $\omega_{\text{obs}}(\theta)$, for a given (sub) sample using the calculator given in Landy & Szalay (1993):

$$\omega_{\text{obs}}(\theta) = \frac{DD(\theta) - 2DR(\theta) + RR(\theta)}{RR(\theta)}, \quad (1)$$

where $DD(\theta)$, $RR(\theta)$, and $DR(\theta)$ are the normalized numbers of galaxy-galaxy, galaxy-random, and random-random pairs, respectively:

$$DD(\theta) = \frac{DD_0(\theta) \times 2}{N_D(N_D - 1)}, \quad (2)$$

$$RR(\theta) = \frac{RR_0(\theta) \times 2}{N_R(N_R - 1)}, \quad (3)$$

$$DR(\theta) = \frac{DR_0(\theta)}{N_D \times N_R}, \quad (4)$$

Here, N is the total number of pairs with subscripts “D” and “R” indicating galaxies and random points, respectively, and subscript “0” indicates the raw number of pairs. We use a random sample composed of 100,000 sources with the same geometrical constraints as the data sample (see figure 2). The 1σ uncertainties in ACF measurements are estimated as:

$$\Delta\omega_{\text{obs}}(\theta) = \sqrt{\frac{1 + \omega(\theta)}{DD_0(\theta)}} \quad (5)$$

following Guaita et al. (2010). While Norberg et al. (2009) find that Poisson errors underestimate the 1σ uncertainties in ACF measurements and that bootstrapping errors overestimate them 40% using a large number of sources ($\sim 10^5$ – 10^6), Khostovan et al. (2017) show that Poisson errors and bootstrapping errors are comparable in the case of a small sample size using ~ 200 H β + [O III] emitters at $z \sim 3.2$ (see also our footnote 4 and figure 5(b)).

We approximate the spatial correlation function of LAEs by a power law:

$$\xi(r) = \left(\frac{r}{r_0}\right)^{-\gamma}, \quad (6)$$

where r , r_0 , and γ are the spatial separation between two objects in comoving scale, the correlation length, and the slope of the power law, respectively (Totsuji & Kihara 1969; Zehavi et al. 2004). We then convert $\xi(r)$ into the ACF, $\omega_{\text{model}}(\theta)$, following Simon (2007), and describe it as:

$$\omega_{\text{model}}(\theta) = C\omega_{\text{model},0}(\theta), \quad (7)$$

where $\omega_{\text{model},0}(\theta)$ is the ACF in the case of $r_0 = 1 \text{ } h_{100}^{-1} \text{ Mpc}$ and C is a normalization constant:

$$C = \left(\frac{r_0 \text{ } h_{100}^{-1} \text{ Mpc}}{1 \text{ } h_{100}^{-1} \text{ Mpc}}\right)^\gamma. \quad (8)$$

The correlation amplitude of the ACF at $\theta = 1''$, A_ω , is

$$A_\omega = C\omega_{\text{model},0}(\theta = 1'') \quad (9)$$

An observationally obtained ACF, $\omega_{\text{obs}}(\theta)$, includes an offset due to the fact that the measurements are made over a limited area. This offset is given by the integral constraint (IC),

$$\omega(\theta) = \omega_{\text{obs}}(\theta) + IC, \quad (10)$$

$$IC = \frac{\Sigma_\theta RR(\theta) C\omega_{\text{model},0}(\theta)}{\Sigma_\theta RR(\theta)}, \quad (11)$$

where $\omega(\theta)$ is the true ACF. We fit the $\omega_{\text{model}}(\theta)$ to this $\omega(\theta)$ over $\sim 40''$ – $1000''$ by minimizing χ^2 :

$$\chi^2 = \Sigma_\theta \left(\frac{\omega_{\text{obs}}(\theta) + IC - \omega_{\text{model}}(\theta)}{\Delta\omega_{\text{obs}}(\theta)} \right)^2 \quad (12)$$

$$= \Sigma_\theta \left(\frac{\omega_{\text{obs}}(\theta) + C(IC_0 - \omega_{\text{model},0}(\theta))}{\Delta\omega_{\text{obs}}(\theta)} \right)^2, \quad (13)$$

where $IC_0 = IC/C$. This θ range is determined conservatively avoiding the one-halo term at small scales and large sampling noise at large scales. We fix γ to the fiducial value 1.8 following previous clustering analyses (e.g., Ouchi et al. 2003). The analytic solution of the best-fit correlation amplitude is

$$A_\omega = \frac{\Sigma_\theta \left(\frac{\omega_{\text{obs}}(\theta)(\omega_{\text{model},0}(\theta) - IC_0)}{\Delta\omega_{\text{obs}}(\theta)^2} \right)}{\Sigma_\theta \left(\frac{IC_0 - \omega_{\text{model},0}(\theta)}{\Delta\omega_{\text{obs}}(\theta)} \right)^2} \omega_{\text{model},0}(\theta = 1''). \quad (14)$$

The 1σ fitting error in A_ω , ΔA_ω , is estimated from $\chi^2_{\text{min}} + 1$, where χ^2_{min} is the minimum χ^2 value. We also derive, for each limiting magnitude, the field-average correlation amplitude over the four survey fields by minimizing the summation of χ^2 over the four fields:

$$A_{\omega, \text{ave}} = \frac{\Sigma_{\theta, i=\text{field}} \left(\frac{\omega_{\text{obs},i}(\theta)(\omega_{\text{model},0}(\theta) - IC_{0,i})}{\Delta\omega_{\text{obs},i}(\theta)^2} \right)}{\Sigma_{\theta, i=\text{field}} \left(\frac{IC_{0,i} - \omega_{\text{model},0}(\theta)}{\Delta\omega_{\text{obs},i}(\theta)} \right)^2} \times \omega_{\text{model},0}(\theta = 1''). \quad (15)$$

The best-fit ACFs are shown in figure 3.

Contaminations by randomly-distributed foreground and background interlopers dilute the apparent clustering amplitude. The correlation amplitude corrected for randomly distributed interlopers, $A_{\omega, \text{corr}}$, is given by

$$A_{\omega, \text{corr}} = \frac{A_\omega}{(1 - f_c)^2}, \quad (16)$$

where f_c is the contamination fraction. The contamination fraction of our LAEs is estimated to be $10 \pm 10\%$ (0–20%) conservatively from the Monte Carlo simulations and the spectroscopic follow-up observations (see section 2.2). This $A_{\omega, \text{corr}}$ is

² In the COSMOS field, Matthee et al. (2016, hereafter M16) find an overdense region in their HAE sample at $z = 2.231 \pm 0.016$ and a part of their survey region overlaps with that of our LAEs at $z = 2.14$ – 2.22 . In their overdense region, two X-ray sources at $z = 2.219$ and $z = 2.232$ have bright Ly α emission. The first one is roughly at the center of the overdense region but just outside of our NB387 image coverage (ID:1139; see figure 2 and table 2 in M16). The second one is included in our coverage but not selected by our color-color criteria probably because its redshift is too large (ID:1037). Indeed, we do not find any overdensity in our LAEs in COSMOS.

the maximum permitted value because interlopers themselves are also clustered in reality. Indeed, some previous clustering studies (e.g., Khostovan et al. 2017) have not applied any contamination correction. In this study, we apply this equation assuming $f_c = 10 \pm 10\%$ so that the error range in $A_{\omega, \text{corr}}$ include both the no correction case and the maximum correction case. The 1σ error in the contamination-corrected correlation amplitude, $\Delta A_{\omega, \text{corr}}$, is derived by summing the 1σ error in the ACF fitting, ΔA_{ω} , and the uncertainty in the contamination estimate, $\Delta f_c = 0.1$, in quadrature (error propagation):

$$\frac{\Delta A_{\omega, \text{corr}}}{A_{\omega, \text{corr}}} \simeq \sqrt{\left(\frac{\Delta A_{\omega}}{A_{\omega}}\right)^2 + \left(\frac{2\Delta f_c}{f_c}\right)^2}. \quad (17)$$

The value of r_0 and its 1σ error are calculated from $A_{\omega, \text{corr}}$ and $\Delta A_{\omega, \text{corr}}$. Table 3 summarizes the results of the clustering analysis.

3.3 Bias Factor

The galaxy-matter bias, b_g , is defined as

$$b_g(r) = \sqrt{\frac{\xi(r)}{\xi_{\text{DM}}(r, z)}}, \quad (18)$$

where $\xi_{\text{DM}}(r, z)$ is the spatial correlation function of underlying dark matter,

$$\xi_{\text{DM}}(r, z) = \int \frac{k^2 dk}{2\pi^2} \frac{\sin(kr)}{kr} P_m(k, z), \quad (19)$$

where $P_m(k, z)$ is the linear dark matter power spectrum as a function of wave number, k , at redshift z (Eisenstein & Hu 1999) with the Eisenstein & Hu (1998) transfer function. We estimate the effective galaxy-matter bias, $b_{g, \text{eff}}$, at $r = 8h_{100}^{-1} \text{Mpc}$ following previous clustering analyses (e.g., Ouchi et al. 2003) using a suite of cosmological codes called Colossus (Diemer & Kravtsov 2015).

Figure 4(a) shows $b_{g, \text{eff}}$ for the cumulative subsamples in the four fields, where $\text{Ly}\alpha$ luminosity limits are calculated from the limiting $NB387$ magnitudes of the subsamples. We find that the average bias value of our LAEs (represented by black stars in panel (a) and also by red stars in panel (b)) does not significantly change with the $\text{Ly}\alpha$ luminosity limit. A possible change in b over $L_{\text{Ly}\alpha} \simeq 3\text{--}10 \times 10^{41} \text{erg s}^{-1}$ is less than 20% since the uncertainties in the average biases are $\sim 10\text{--}20\%$.

This weak dependence may be partly due to radiative transfer effects on $\text{Ly}\alpha$ photons. Star forming galaxies in more massive (i.e., larger bias) halos are thought to have higher $SFRs$ and thus brighter nebular emission lines. Indeed, Cochrane et al. (2017) have found a significant positive correlation between $\text{H}\alpha$ luminosity and bias for bright $z = 2.23$ HAEs, indicating a similarly strong correlation between intrinsic $\text{Ly}\alpha$ luminosity and bias for bright galaxies. However, such a strong correlation, if any, weakens when observed $\text{Ly}\alpha$ luminosity is used in place, because brighter (i.e., more massive) galaxies have lower

$\text{Ly}\alpha$ escape fractions, $f_{\text{esc}}^{\text{Ly}\alpha}$ (e.g., Vanzella et al. 2009; Matthee et al. 2016). Indeed, our cumulative subsamples do not show a significant correlation between the observed $\text{Ly}\alpha$ luminosity and the total SFR (derived from SED fitting in the same manner as described in section 4) but rather show a positive correlation between the observed $\text{Ly}\alpha$ luminosity and the $\text{Ly}\alpha$ escape fraction, where the intrinsic $\text{Ly}\alpha$ luminosity is calculated from the total SFR (Brocklehurst 1971; Kennicutt 1998).

Moreover, some previous studies have found that high-redshift UV-selected galaxies with comparably faint UV luminosities (L_{UV}) to our LAEs (the average absolute magnitude of our LAEs is $M_{\text{UV}} \sim -19$ mag) have weak dependence of b_g on UV luminosity ($z \sim 3\text{--}4$ Lyman break galaxies (LBGs): Ouchi et al. 2004, 2005; Harikane et al. 2016; Bielby et al. 2016, see however, Lee et al. (2006) who find significant dependence for $z \sim 4\text{--}5$ LBGs), suggesting that the correlation between intrinsic $\text{Ly}\alpha$ luminosity and bias is not so strong for typical LAEs with modest $\text{Ly}\alpha$ luminosities.

The faintest limiting $\text{Ly}\alpha$ luminosity at which $b_{g, \text{eff}}$ measurements are available for all four fields is $L_{\text{Ly}\alpha} = 6.2 \times 10^{41} \text{erg s}^{-1}$ (corresponding to 25.5 mag in $NB387$). In order to reduce the uncertainty due to cosmic variance as much as possible, we adopt the average $b_{g, \text{eff}}$ at this limiting luminosity, $b_{g, \text{eff}}^{\text{ave}} = 1.22^{+0.16}_{-0.18}$, as the average $b_{g, \text{eff}}$ of our entire sample.

This average bias is lower than that of the previous work on narrow-band-selected LAEs at $z \sim 2.1$, $b_{g, \text{eff}} = 1.8 \pm 0.3$ (Guaita et al. 2010, see the blue point in panel (b) of figure 4), with a probability of 96%. The median $\text{Ly}\alpha$ luminosity of their sample is $L_{\text{Ly}\alpha} = 1.3 \times 10^{42} \text{erg s}^{-1}$ and their 5σ detection limit in $\text{Ly}\alpha$ luminosity is $L_{\text{Ly}\alpha} = 6.3 \times 10^{41} \text{erg s}^{-1}$, which is similar to the luminosity limit of our $NB387 \leq 25.5$ samples. Our clustering method is essentially the same as of Guaita et al. (2010) and in both studies the bias value is calculated at $r = 8h_{100}^{-1} \text{Mpc}$. Although we use a slightly different cosmological parameter set, $(\Omega_m, \Omega_\Lambda, h, \sigma_8) = (0.3, 0.7, 0.7, 0.8)$, from theirs, $(\Omega_m, \Omega_\Lambda, h, \sigma_8) = (0.26, 0.74, 0.7, 0.8)$, using Guaita et al. (2010)'s set changes $b_{g, \text{eff}}$ only negligibly. Our contamination fraction, $f_c = 10 \pm 10\%$, is comparable to or slightly conservative than theirs, $f_c = 7 \pm 7\%$. The error in Guaita et al. (2010)'s $b_{g, \text{eff}}$ is a quadrature sum of the uncertainty in f_c and the fitting error (statistical error), with the latter dominating because of the small sample size (250 objects). As discussed in section 3.4, their high $b_{g, \text{eff}}$ value is attributable to cosmic variance since their survey area is approximately one third of ours (see figure 5(b)). Indeed, the sky distribution of their LAEs has a large scale excess at the north-west part and the ACF measurements seem to deviate to higher values from the best-fit power law at large scales because of it³.

³ We do not include the result of Guaita et al. (2010) when calculating the average bias.

Table 3. Clustering Measurements of our LAEs.

Field $NB387_{\text{tot}}$ (mag)	A_ω	$A_{\omega, \text{corr}}$	r_0 (h_{100}^{-1} Mpc)	$b_{g, \text{eff}}$	M_h ($\times 10^{10} M_\odot$)	reduced χ^2_ν	IC
	(1)	(2)	(3)	(4)	(5)	(6)	(7)
SXDS							
≤ 25.0	4.70 ± 2.86	5.80 ± 3.75	$2.78^{+0.89}_{-1.22}$	$1.40^{+0.40}_{-0.57}$	$10.1^{+28.8}_{-10.1}$	1.74	0.0137
≤ 25.3	2.07 ± 1.27	2.56 ± 1.67	$1.77^{+0.57}_{-0.78}$	$0.93^{+0.27}_{-0.38}$	$0.4^{+3.2}_{-0.4}$	5.40	0.0060
≤ 25.5	3.35 ± 0.78	4.14 ± 1.33	$2.31^{+0.39}_{-0.45}$	$1.18^{+0.18}_{-0.21}$	$3.3^{+5.2}_{-2.7}$	3.02	0.0097
COSMOS							
≤ 25.0	3.88 ± 3.03	4.79 ± 3.88	$2.50^{+0.98}_{-1.51}$	$1.27^{+0.44}_{-0.72}$	$5.5^{+25.3}_{-5.5}$	0.89	0.0176
≤ 25.3	4.44 ± 1.81	5.48 ± 2.54	$2.70^{+0.64}_{-0.79}$	$1.36^{+0.29}_{-0.36}$	$8.5^{+16.6}_{-7.7}$	1.11	0.0201
≤ 25.5	3.32 ± 1.25	4.10 ± 1.79	$2.29^{+0.51}_{-0.63}$	$1.18^{+0.23}_{-0.29}$	$3.1^{+7.5}_{-2.9}$	0.62	0.0150
≤ 25.8	3.70 ± 0.70	4.57 ± 1.33	$2.44^{+0.37}_{-0.42}$	$1.24^{+0.17}_{-0.20}$	$4.7^{+6.0}_{-3.5}$	0.95	0.0168
HDFN							
≤ 25.0	6.89 ± 3.77	8.51 ± 5.03	$3.44^{+1.01}_{-1.35}$	$1.70^{+0.44}_{-0.61}$	$29.3^{+55.5}_{-27.6}$	0.81	0.0319
≤ 25.3	9.55 ± 2.28	11.79 ± 3.84	$4.13^{+0.70}_{-0.81}$	$2.00^{+0.30}_{-0.36}$	$62.9^{+52.0}_{-38.3}$	1.33	0.0441
≤ 25.5	5.18 ± 1.51	6.40 ± 2.34	$2.94^{+0.56}_{-0.66}$	$1.47^{+0.25}_{-0.30}$	$13.6^{+17.7}_{-10.5}$	0.95	0.0240
≤ 25.8	2.52 ± 0.75	3.11 ± 1.15	$1.97^{+0.38}_{-0.45}$	$1.03^{+0.18}_{-0.21}$	$1.0^{+2.6}_{-0.9}$	1.12	0.0116
CDFS							
≤ 25.0	3.78 ± 11.89	4.67 ± 14.72	$2.47^{+2.97}_{-2.47}$	$1.26^{+1.30}_{-1.26}$	$5.0^{+170.0}_{-5.0}$	0.71	0.0215
≤ 25.3	5.43 ± 8.12	6.70 ± 10.14	$3.02^{+2.02}_{-3.02}$	$1.51^{+0.88}_{-1.51}$	$15.5^{+117.8}_{-15.5}$	0.61	0.0309
≤ 25.5	5.47 ± 6.34	6.75 ± 7.97	$3.03^{+1.64}_{-3.03}$	$1.51^{+0.72}_{-1.51}$	$15.8^{+85.5}_{-15.8}$	1.07	0.0311
≤ 25.8	2.61 ± 3.43	3.22 ± 4.29	$2.01^{+1.21}_{-2.01}$	$1.04^{+0.55}_{-1.04}$	$1.2^{+20.0}_{-1.2}$	0.94	0.0148
≤ 26.3	8.62 ± 1.49	10.64 ± 2.99	$3.90^{+0.58}_{-0.65}$	$1.90^{+0.25}_{-0.29}$	$50.2^{+35.9}_{-28.0}$	1.66	0.0490
field average (number of fields)							
≤ 25.0 (4)	4.69 ± 1.70	5.80 ± 2.46	$2.78^{+0.60}_{-0.74}$	$1.40^{+0.27}_{-0.34}$	$10.1^{+17.0}_{-8.8}$	0.75	
≤ 25.3 (4)	4.04 ± 0.90	4.99 ± 1.57	$2.56^{+0.42}_{-0.48}$	$1.30^{+0.19}_{-0.22}$	$6.3^{+8.3}_{-4.8}$	2.04	
≤ 25.5 (4)	3.55 ± 0.58	4.39 ± 1.21	$2.38^{+0.34}_{-0.39}$	$1.22^{+0.16}_{-0.18}$	$4.0^{+5.1}_{-2.9}$	1.01	
≤ 25.8 (3)	2.75 ± 0.45	3.40 ± 0.94	$2.07^{+0.30}_{-0.34}$	$1.07^{+0.14}_{-0.16}$	$1.5^{+2.4}_{-1.2}$	1.08	
≤ 26.3 (1)	8.62 ± 1.49	10.64 ± 2.99	$3.90^{+0.58}_{-0.65}$	$1.90^{+0.25}_{-0.29}$	$50.2^{+35.9}_{-28.0}$	1.66	

Note. (1) The best fit correlation amplitude without f_c correction; (2) the best fit correlation amplitude with f_c correction used to derive (3)–(5); (3) the best fit correlation length; (4) the best fit effective bias factor; (5) the best fit effective dark matter halo mass; (6) reduced chi-squared value; (7) the best fit integral constant; The value in parentheses shows the number of fields used to calculate the field-average correlation amplitude using equation 15.

3.4 Cosmic Variance on Bias Factor

Our average effective bias value and that of Guaita et al. (2010) are not consistent within the 1σ uncertainties in spite of similar limiting $\text{Ly}\alpha$ luminosities. Biases derived from limited survey areas possibly suffer from cosmic variance due to spatial variations in the ACF of dark matter. We analytically estimate cosmic variance in the bias value derived from clustering analysis for the first time. With the ACF the galaxy-matter bias can be expressed as $b(\theta) = \sqrt{\omega_{\text{gal}}(\theta)/\omega_{\text{DM}}(\theta)}$. Assuming that the cosmic variance in b originates solely from the spatial variation of the dark matter ACF, we can express the b of a given galaxy sample in a given survey field as:

$$b(\text{field}) = \sqrt{\frac{\omega_{\text{DM}}(\text{field})}{\langle \omega_{\text{DM}} \rangle} \frac{\omega_{\text{gal}}(\text{field})}{\omega_{\text{DM}}(\text{field})}} = \sqrt{\frac{\omega_{\text{DM}}(\text{field})}{\langle \omega_{\text{DM}} \rangle}} b_{\text{int}}, \quad (20)$$

where $\langle \omega_{\text{DM}} \rangle$ is the cosmic average of the dark matter ACF, $\omega_{\text{DM}}(\text{field})$ is the dark matter ACF in the field, $\omega_{\text{gal}}(\text{field})$ is the observed galaxy ACF in the field, and

$$b_{\text{int}} \equiv \sqrt{\frac{\omega_{\text{gal}}(\text{field})}{\omega_{\text{DM}}(\text{field})}} \quad (21)$$

is the intrinsic bias of this galaxy population which we assume to be unchanged from field to field (parameter θ is omitted for clarity). This assumption is the same as the one assumed to predict cosmic variance in number density (e.g., Moster et al. 2011), as explained below. Field to field fluctuations of number density, $\sigma_{\text{ND}, g'}$, are assumed to come from field to field fluctuations of dark matter distribution (i.e., cosmic variance in the density of dark matter), $\sigma_{\text{ND}, \text{DM}}$, as

$$\sigma_{\text{ND}, g'} = b_{g'} \sigma_{\text{ND}, \text{DM}}, \quad (22)$$

where the intrinsic galaxy bias, $b_{g'}$, is uniform and independent of fields by definition. We also assume that $\omega_{\text{gal}}^2(\text{field})$ is proportional to $\omega_{\text{DM}}^2(\text{field})$ by a factor of b_{int} .

The covariance in ω_{DM} between two angular separations for area Ω_s is given by the first term of equation 19 of Cohn (2009)⁴:

⁴ Cohn (2009)'s equation (19) corresponds to the full covariance including those due to a discrete sampling with a finite number of objects; the second term is proportional to $P_2(K)/N\Omega_s$, where N is the number density of objects, and the subsequent terms correspond to the uncertainty shown in our equation 5. Inclusion of the second term in our equation 23 increases

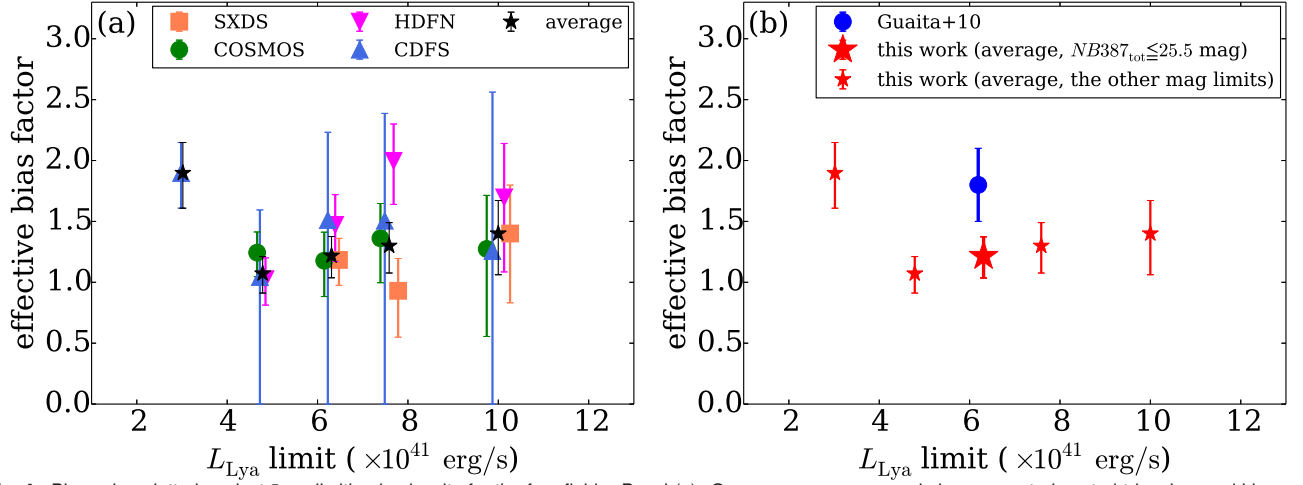


Fig. 4. Bias value plotted against $L_{\text{Ly}\alpha}$ limiting luminosity for the four fields. Panel (a). Orange squares, green circles, magenta inverted triangles, and blue triangles represent the SXDS, COSMOS, HDFN, and CDFS fields, respectively. Black stars indicate the average (weighted mean) over available fields at each limiting luminosity (also shown by red stars in panel (b)). For presentation purposes, we slightly shift all of the points except for black stars along the abscissa. Panel (b). The measurements shown by small black stars in panel (a) are plotted by small red stars except for the value at $L_{\text{Ly}\alpha} \text{ limit} \simeq 6 \times 10^{41} \text{ erg s}^{-1}$ (or $NB387_{\text{tot}} \leq 25.5 \text{ mag}$) shown by a large red star. Guaita et al. (2010)'s measurement is also plotted by a blue circle. (Color online)

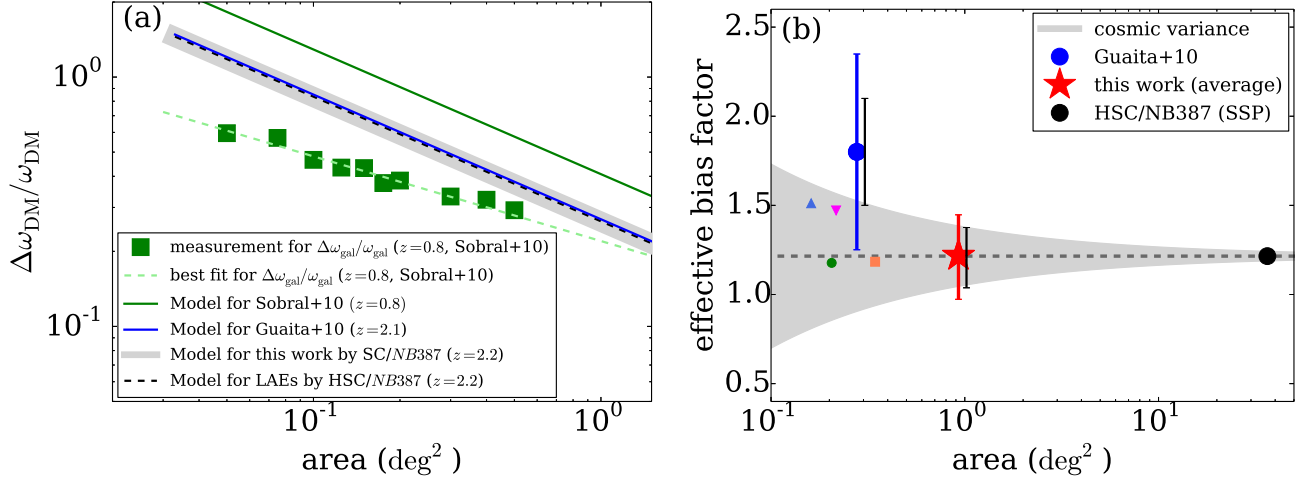


Fig. 5. Cosmic variance on clustering analysis. Panel (a). Uncertainties in the amplitude of the dark matter ACF as a function of survey area. Green squares and a light green dashed line denote the empirical measurements at $z \sim 0.8$ and the best-fit power law to them, respectively, by Sobral et al. (2010, : $\Delta\omega_{\text{gal}}/\omega_{\text{gal}}$). Other lines show our analytic calculations for four NB surveys: green solid line for Sobral et al. (2010), lightgray thick solid line for this study (Suprime-Cam/ $NB387$), blue solid line for Guaita et al. (2010), and black dashed line for an on-going Hyper Suprime-Cam/ $NB387$ survey (see section 6.5). Panel (b). Effective bias factor as a function of survey area. The cosmic variance on $b_{\text{g,eff}}^{\text{ave}}$, which is indicated by a light gray thick solid line in panel (a), is shown by a light gray filled region around $b_{\text{g,eff}}^{\text{ave}}$ (fixed) shown by a dim gray dashed line. A red star and a blue circle indicate the $b_{\text{g,eff}}^{\text{ave}}$ in this work and the $b_{\text{g,eff}}$ in Guaita et al. (2010), respectively, where colored error bars include the uncertainty due to cosmic variance while black bars next to them do not. A black circle corresponds to the HSC/ $NB387$ survey when completed. A small orange square, green circle, magenta inverted triangle, and blue triangle represent $b_{\text{g,eff}}$ with $NB387 \leq 25.5 \text{ mag}$ from SXDS, COMOS, HDFN, and CDFS, respectively. (Color online)

$$\begin{aligned} & \text{Cov}(\omega_{\text{DM}}(\theta), \omega_{\text{DM}}(\theta')) \\ &= \frac{1}{\pi\Omega_s} \int K \, dK J_0(K\theta) J_0(K\theta') P_2^2(K), \end{aligned} \quad (23)$$

where K , $P_2(K)$ and $J_0(K\theta)$ are the Fourier transform of θ , the projected power spectrum calculated using the redshift distribution defined by the filter, and the zeroth-order Bessel function of the first kind, respectively. With this equation we calculate ω_{DM} and its standard deviation, σ_{DM} , for the three angular bins

$\Delta\omega_{\text{DM}}$ by $\sim 30\%$ for our LAE survey, although in this study we neglect this term and only consider cosmic variance not dependent on N .

used to determine the A_ω of our LAEs. We then fit a power-law correlation function to those values in the same manner as for observed data but also considering the intrinsic covariance given in equation (23), and obtain the relative uncertainty in A_ω due to the variation in ω_{DM} , $\frac{\Delta\omega_{\text{DM}}}{\omega_{\text{DM}}}$. According to equation 23, the relative uncertainty in A_ω depends on Ω_s as:

$$\frac{\Delta\omega_{\text{DM}}}{\omega_{\text{DM}}} \propto \Omega_s^{-0.5}, \quad (24)$$

as shown by a light gray solid line in figure 5 (a).

We find $\frac{\Delta\omega_{\text{DM}}}{\omega_{\text{DM}}} \simeq 53\%$ for $\Omega_s = 0.25 \text{ deg}^2$, a typical area of

the four survey fields, and $\simeq 26\%$ for the entire survey area ($\simeq 1 \text{ deg}^2$).

Sobral et al. (2010) have empirically estimated relative uncertainties in ACF measurements for NB-selected $z = 0.85$ HAEs as a function of area by dividing their survey regions, $\simeq 1.3 \text{ deg}^2$ in total, into sub regions with different sizes (green squares in figure 5(a)). This empirical relation has been used to estimate cosmic variance in ACF measurements in a $\simeq 2 \text{ deg}^2$ survey area of emission line galaxies at $z \sim 0.8\text{--}4.7$ in Khostovan et al. (2017). Our analytic method applied to the Sobral et al. (2010) survey with their own NB filter (over the same fitting range of θ as that for our LAEs for simplicity), however, gives larger uncertainties as shown by a green solid line in figure 5(a). This may be partly because the area of Sobral et al. (2010)'s survey is not large enough to catch the total variance. Our analytic estimation seems to be more conservative than theirs.

We expect that Guaita et al. (2010)'s b obtained from $\sim 0.28 \text{ deg}^2$ area has also a $\simeq 51\%$ uncertainty using their $NB3727$ filter (solid blue line). The 1σ uncertainty in an observed bias including cosmic variance, $\Delta b_{g, \text{eff}, \text{CV}}$, is given by:

$$\frac{\Delta b_{g, \text{eff}, \text{CV}}}{b_{g, \text{eff}}} \simeq \frac{1}{2} \sqrt{\left(\frac{\Delta A_\omega}{A_\omega}\right)^2 + \left(\frac{2\Delta f_c}{f_c}\right)^2 + \left(\frac{\Delta \omega_{\text{DM}}}{\omega_{\text{DM}}}\right)^2} \quad (25)$$

$$\simeq \frac{1}{2} \sqrt{\left(\frac{2\Delta b_{g, \text{eff}}}{b_{g, \text{eff}}}\right)^2 + \left(\frac{\Delta \omega_{\text{DM}}}{\omega_{\text{DM}}}\right)^2}, \quad (26)$$

where $\Delta b_{g, \text{eff}}$ is the 1σ error in $b_{g, \text{eff}}$.

By updating the errors using this equation (where for our $b_{g, \text{eff}}$ the plus and minus errors are treated separately), our average effective bias and that of Guaita et al. (2010) are written as $b_{g, \text{eff}}^{\text{ave}} = 1.22^{+0.23}_{-0.26}$ and $b_{g, \text{eff}} = 1.8 \pm 0.55$, respectively, thus becoming consistent with each other (see figure 5 (b)). We also note that the relatively large scatter of b among the four fields at each limiting $\text{Ly}\alpha$ luminosity seen in figure 4(a) may be partly due to cosmic variance although the observational errors are too large to confirm it (see figure 5 (b)). All the best-fit b values for the four fields fall within the 1σ uncertainty range from cosmic variance shown by a shaded light gray region in figure 5 (b).

3.5 Dark Matter Halo Mass

We estimate effective dark matter halo masses from $b_{g, \text{eff}}$ directly assuming that each halo hosts only one galaxy and that our sample has a narrow range of dark matter halo mass. We use the formula of bias and peak height in the linear density field, ν , given in Tinker et al. (2010), which is based on a large set of collisionless cosmological simulations in flat ΛCDM cosmology. The obtained ν is converted to the effective dark matter halo mass with the top-hat window function and the linear dark matter power spectrum (Eisenstein & Hu 1998, 1999) using a

cosmological package for Python called CosmoloPy⁵.

The effective halo mass of each sub-sample is listed in table 3. The field average of effective halo masses corresponding to the field average of effective biases of our LAEs with $NB387_{\text{tot}} \leq 25.5 \text{ mag}$, $b_{g, \text{eff}}^{\text{ave}} = 1.22^{+0.16}_{-0.18}$, is $4.0^{+5.1}_{-2.9} \times 10^{10} M_\odot$. This value is roughly comparable to previous measurements for $z \sim 3\text{--}7$ LAEs with similar $\text{Ly}\alpha$ luminosities, $M_h \simeq 10^{10}\text{--}10^{12} M_\odot$ (e.g., Ouchi et al. 2005, 2010; Kovač et al. 2007; Gawiser et al. 2007; Shioya et al. 2009; Bielby et al. 2016; Diener et al. 2017; Ouchi et al. 2017), suggesting that the mass of dark haloes which can host typical LAEs is roughly unchanged with time.

The average M_h of our LAEs is smaller than those of HAEs at $z \sim 1.6$ (Kashino et al. 2017), $M_h \sim 7 \times 10^{12} M_\odot$, and at $z \sim 2.2$, a few times $10^{12} M_\odot$ (Cochrane et al. 2017). The typical dust-corrected $\text{H}\alpha$ luminosity, $L_{\text{H}\alpha, \text{corr}}$, of our LAEs is estimated to be $4.3 \pm 0.9 \times 10^{41} \text{ erg s}^{-1}$ from the SFR obtained by SED fitting in section 4 using the conversion formula given in Kennicutt (1998) on the assumption of case B recombination. This $\text{H}\alpha$ luminosity corresponds to an effective halo mass of $M_{h, \text{eff}} = 5.2^{+4.8}_{-2.7} \times 10^{10} M_\odot$ according to the redshift independent relation between the normalized luminosity $L_{\text{H}\alpha, \text{corr}}/L_{\text{H}\alpha}^*(z)$ and $M_{h, \text{eff}}$ found by Cochrane et al. (2017). The estimated halo mass of our LAEs, $M_h = 4.0^{+5.1}_{-2.9} \times 10^{10} M_\odot$, is thus consistent with this relation. This result supports the result by Shimakawa et al. (2017) and Hagen et al. (2016) that the stellar properties of LAEs at $z \sim 2\text{--}3$ do not significantly differ from those of other emission galaxies such as HAEs and [O III] emitters. However, Cochrane et al. (2017) assume a constant dust attenuation against $\text{H}\alpha$ luminosity, $A_{\text{H}\alpha} = 1.0 \text{ mag}$, for all HAEs, which is larger than that of our LAEs, $A_{\text{H}\alpha} \sim 0.13 \pm 0.04 \text{ mag}$, derived from the average $E(B - V)$ in section 4. If the (extrapolated) relation overestimates $L_{\text{H}\alpha, \text{corr}}$ at low halo masses owing to overestimation of $A_{\text{H}\alpha}$, then the true log-log slope of $L_{\text{H}\alpha, \text{corr}}$ as a function of M_h would be steeper, implying that our LAEs would lie above the relation (see also section 5.2 and figure 10).

4 SED fitting

We derive stellar population parameters of LAEs with $NB_{\text{tot}} \leq 25.5 \text{ mag}$ in each of the four fields by SED fitting to stacked multiband images. This threshold magnitude is the same as that adopted in the clustering analysis to define average halo masses. We only use 170 objects ($\sim 14\%$ of the entire sample, 1248) which have data in ten broadbands ($B, V, R, i, z, J, H, K, \text{ch1}$, and ch2) and which are not contaminated by other objects in the IRAC images (sec. 2.1 and tabel 2). The procedure to select ‘IRAC-clean’ objects is described in the next subsection.

⁵ <http://roban.github.com/CosmoloPy/>

Table 4. Results of SED fitting.

field	M_* ($10^8 M_\odot$)	$E(B-V)_*$ [A_{1600}] (mag)	Age (10^8 yr)	SFR ($M_\odot \text{yr}^{-1}$)	χ_r^2
	(1)	(2)	(3)	(4)	(5)
SXDS	$9.7^{+3.6}_{-1.7}$	$0.05^{+0.01}_{-0.02}$ [$0.6^{+0.1}_{-0.2}$]	$3.6^{+2.8}_{-1.1}$	$3.3^{+0.5}_{-0.7}$	0.604
COSMOS	$14.0^{+3.4}_{-3.6}$	$0.07^{+0.02}_{-0.02}$ [$0.8^{+0.2}_{-0.2}$]	$4.1^{+2.4}_{-1.8}$	$4.2^{+1.2}_{-0.8}$	0.473
HDFN	$7.6^{+4.0}_{-1.9}$	$0.06^{+0.02}_{-0.03}$ [$0.7^{+0.2}_{-0.4}$]	$3.2^{+4.0}_{-1.4}$	$2.9^{+0.8}_{-0.8}$	1.298
CDFS	$10.3^{+11.1}_{-9.7}$	$0.02^{+0.07}_{-0.01}$ [$0.2^{+0.8}_{-0.1}$]	$5.7^{+8.6}_{-5.7}$	$2.2^{+5.3}_{-0.4}$	0.120
Average	10.2 ± 3.0	0.06 ± 0.02 [0.6 ± 0.2]	3.8 ± 0.6	3.4 ± 0.7	

Note. (1) The best fit stellar mass; (2) the best-fit color excess [UV attenuation]; (3) the best fit age; (4) the best fit SFR; (5) reduced chi-squared value. The UV attenuation is derived from a SMC-like attenuation curve. Metallicity, redshift, and $f_{\text{esc}}^{\text{ion}}$ are fixed to $0.2Z_\odot$, 2.18, and 0.2, respectively.

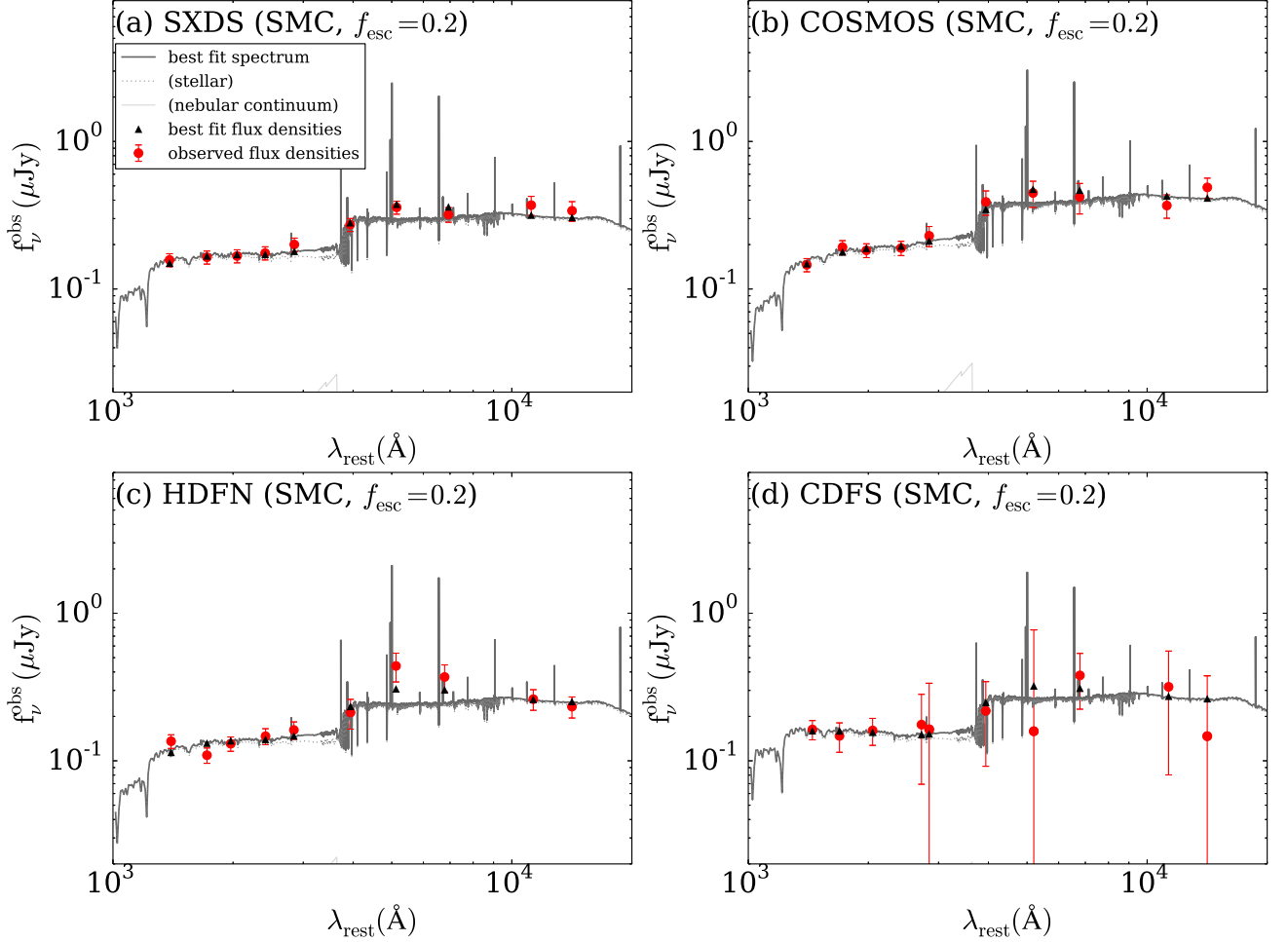


Fig. 6. Results of SED fitting to stacked LAEs with $NB387_{\text{tot}} \leq 25.5$ mag in the SXDS, COSMOS, HDFN, and CDFS fields from panels (a) to (d). For each panel, a gray solid line, a light gray dotted line, and a light gray solid line show the best-fit model spectrum, its stellar component, and its nebular component, respectively. Red filled circles and black filled triangles represent the observed flux densities and the flux densities calculated from the best-fit spectrum, respectively. (Color online)

4.1 Selection of IRAC-clean Objects

The IRAC images have much worse spatial resolutions (i.e., larger FWHMs of the PSF) compared with the other band images. Moreover, they have large-scale residual backgrounds (contaminated surrounding skies) around bright objects and in crowded regions due to the extended PSF profile of IRAC. Contaminations by nearby objects and by large-scale sky resid-

uals can give significant systematic errors in the photometry of stacked images because our LAEs are expected to have very low stellar masses, or very faint IRAC magnitudes. To minimize these contaminations, we select clean LAEs by two steps.

First, we exclude all LAEs which have one or more neighbors. On a reasonable assumption that objects bright in IRAC are similarly bright in K , we exclude all LAEs which have one

or more K -detected object with a separation between $0.''85$ and $4.''5$; an object within $0.''85$ separation is considered to be the counterpart to the LAE conservatively (the typical separation is $\sim 0.''2$). $4.''5$ is 2.5 times larger than the PSF size of the ch1. The K -detected catalogs given in section 2.3 are used.

Second, we exclude all LAEs with a high sky background in the following manner. For each field, we randomly select 5,000 positions with no K -band objects within $4.''5$ (i.e., passing the first step) and measure the sky background in an annular region of $3.''5$ radius centered at these positions. We then make a histogram of these sky background values, which is skewed toward higher values because of contaminations by bright or crowded objects outside of $4.''5$ radius. We fit a Gaussian to the low-flux side (including the peak) of the histogram and obtain its average, μ_{rand} , which we consider to be the true sky background. If cutout images at all the random positions are median-stacked, its annular-region sky background will be brighter than μ_{rand} . A similar systematic sky-background difference will also be seen when all LAEs are stacked, possibly introducing some systematic errors in photometry. The sky background of the median-stacked random image becomes equal to μ_{rand} if positions whose sky background is higher than a certain threshold, sky_{thres} , are removed, where sky_{thres} can be determined so that the total number of the remaining positions is twice as large as the number of positions below μ_{rand} . Thus, we conservatively remove LAEs with a higher annular-region sky background than sky_{thres} , and are left with 93, 21, 56, and 4 IRAC-clean LAEs in SXDS, COSMOS, HSFN and CDFS, respectively. The stacked flux densities of the IRAC-clean LAEs in the B to K bands are mostly consistent with those of the all LAEs before cleaning.

4.2 Stacking Analysis and Photometry

We perform a stacking analysis for each subsample in almost the same manner as Nakajima et al. (2012) and Kusakabe et al. (2015). $50'' \times 50''$ images are cut out at the position of LAEs in the $NB387$ image with IRAF/imcopy task. In SXDS field, for each of the B to K bands, PSFs are matched to the worst one among the SXDS-Center, North, and South sub-fields using IRAF/gauss task (see table 1). We perform $NB387$ -centered median image-stacking to these images using IRAF/imcombine task. Although a stacked SED is not necessarily a good representation of individual objects (Vargas et al. 2014), stacking is still useful for our faint objects to obtain an SED covering rest-frame $\sim 1000\text{--}10000 \text{ \AA}$.

An aperture flux is measured for each stacked image using the PyRAF/phot task. Following Ono et al. (2010a), we use an aperture diameter of $2''$ for the $NB387$, optical, and NIR band images and $3''$ for the MIR (IRAC) images. For the $NB387$ - to K -band images, the inner radius of the annulus to

measure the sky flux is set to twice the FWHM of the largest PSF among these images⁶, and the area of the annulus is set to five times larger than that of the aperture. For each of the ch1 and ch2 images, we obtain the net $3''$ -aperture flux density of LAEs by subtracting the offset between the annular-region and $3''$ -aperture flux densities of the stacked image of IRAC-clean random positions generated in the previous subsection, from the $3''$ -aperture flux density of the LAE image (output of the PyRAF/phot task)⁷.

We use the original zero-point magnitudes (ZP) in the references although some previous work argues that some ZPs need to be corrected (e.g., Yagi et al. 2013; Skelton et al. 2014). This is because the direction of the correction given by Yagi et al. (2013) is opposite to that by Skelton et al. (2014) in optical bands in the SXDS field. All aperture magnitudes are corrected for Galactic extinction, $E(B - V)_b$, of 0.020, 0.018, 0.012, and 0.008 for the SXDS, COSMOS, HSFN, and CDFS fields, respectively (Schlegel et al. 1998).

The aperture magnitudes are then converted into total magnitudes using the aperture correction values summarized in table 1 (see also section 2.3). The stacked SEDs thus obtained for individual subsamples are shown in figure 6. The errors include photometric errors and errors in aperture correction and the ZP. For the ch1 and ch2 data, errors in sky subtraction, $\sim 0.02\text{--}0.17$ mag, are also included. The photometric errors are determined following the procedure of Kusakabe et al. (2015). The aperture correction errors in the $NB387$, optical, and NIR bands are estimated to be less than 0.03 mag, and those in the ch1 and ch2 bands are set to 0.05 mag. We conservatively adopt 0.1 mag as the ZP error for all bands.

4.3 SED Models

We perform SED fitting on the stacked SEDs to derive stellar population parameters in a similar manner to Kusakabe et al. (2015). Nebular emission (lines and continuum) is added to the stellar population synthesis model of GALAXEV with constant star formation history and $0.2Z_{\odot}$ stellar metallicity following previous SED studies of LAEs (Bruzual & Charlot 2003; Ono et al. 2010a; Vargas et al. 2014). We assume a SMC extinction curve as the attenuation curve (hereafter a SMC-like attenuation curve; Gordon et al. 2003), which is suggested to be more appropriate for LAEs at $z \sim 2$ than the Calzetti curve (Calzetti et al. 2000) by Kusakabe et al. (2015) and for star forming

⁶ The PSF size of the CDFS H -band image is exceptionally large and we determine the radius of the annulus for this image independently.

⁷ The sky background value on a $3.''5$ -radius annulus placed at the image center is consistent between the stacked LAE images and the stacked images of IRAC-clean random positions. For stacked images of random positions, annular-region sky flux densities are brighter than aperture-region sky flux densities with differences corresponding to $\sim 7\text{--}28\%$ of the aperture fluxes of median-stacked LAEs.

galaxies at $z \geq 2$ by Reddy et al. (2017)⁸. We also examine the cases of the Calzetti curve for comparison (see appendix 1.1). We also assume $E(B - V)_{\text{gas}} = E(B - V)_*$ (Erb et al. 2006). The Lyman continuum escape fraction, $f_{\text{esc}}^{\text{ion}}$, is fixed to 0.2 considering recent observations of $f_{\text{esc}}^{\text{ion}} \sim 0.1\text{--}0.3$ for $z \sim 3$ LAEs by Nestor et al. (2013)⁹. This means that 80% of ionizing photons produced are converted into nebular emission (see Ono et al. 2010a).

For each field's stacked SED we search for the best-fitting model SED that minimizes χ^2 and derive the following stellar parameters: stellar mass (M_*), color excess $E(B - V)_*$ or UV attenuation of A_{1600} , age, and SFR . Stellar masses are calculated by solving $\frac{\partial \chi^2}{\partial M_*} = 0$ since it is the amplitude of the model SED. SFR is not a free parameter in the fit but determined from M_* and age and thus the degree of freedom is 7. The 1σ confidence interval in these stellar parameters is estimated from $\chi_{\text{min}}^2 + 1$, where χ_{min}^2 is the minimum χ^2 value.

4.4 Results of SED Fitting

Table 4 summarizes the best-fit parameters and figure 6 compares the best-fit SEDs with the observed ones. The mean of the parameters over the four fields is: $M_* = 10.2 \pm 3.0 \times 10^8 M_\odot$, $A_{1600} = 0.6 \pm 0.2$ mag, Age = $3.8 \pm 0.6 \times 10^8$ yr, and $SFR = 3.4 \pm 0.7 M_\odot \text{ yr}^{-1}$. We discuss the infrared excess and the star formation mode in the following subsections using the results with a SMC-like curve.

Not only a SMC-like but also the Calzetti attenuation curve fits the data well but the resulting parameter values are different (see Appendix 1.1 and figure 13). The Calzetti curve tends to give a smaller stellar mass, a higher attenuation, a younger age, and a higher SFR as the best fit value compared with a SMC-like curve. The difference in the average stellar mass is a factor of ~ 3 but that in the average SFR reaches a factor of ~ 4 .

4.4.1 M_* – IRX relation

As shown in figure 7, galaxies with higher stellar masses tend to have higher infrared excesses, $IRX \equiv L_{\text{IR}}/L_{\text{UV}}$, where L_{IR} is the IR luminosity (see also footnote 10), which is an indicator of dustiness (the consensus relation: Reddy et al. 2010; Whitaker et al. 2014; Bouwens et al. 2016). The dust emission of typical LAEs with $M_* \sim 10^9 M_\odot$ is too faint to be detected, although a few LAEs at $z \sim 2\text{--}3$ are detected by Hersche/PACS and Spitzer/MIPS (e.g., Pentericci et al. 2010; Oteo et al. 2012).

⁸ While Hagen et al. (2017) have found that the SMC indeed has a flatter extinction curve in average than the classical (Pei 1992; Gordon et al. 2003) curve, we adopt the classical curve which is consistent with recent observations of high- z galaxies including LAEs. Reddy et al. (2017) find that galaxies at $z = 1.5\text{--}2.5$ prefer a SMC-like attenuation curve combined with sub-solar metallicity stellar population models.

⁹ We also perform SED fitting with models without nebular emission, $f_{\text{esc}}^{\text{ion}} = 1$, to examine to what extent SFR s and M_* change in appendix 1.2.

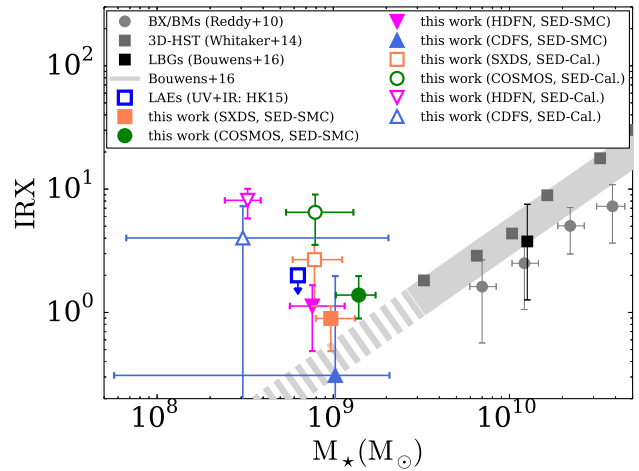


Fig. 7. IRX vs M_* . Dim gray squares, a black square, and a light gray solid band represent, respectively, 3D-HST galaxies at $z \sim 2$ in Whitaker et al. (2014), UV selected galaxies at $z \sim 2$ in Reddy et al. (2010), LBGs at $z \sim 2\text{--}3$ in Bouwens et al. (2016), and the consensus relation of them determined by Bouwens et al. (2016), with its extrapolation indicated by a gray striped band (see also footnote 1). A filled orange square, green circle, magenta inverted triangle, and blue triangle indicate the SXDS, COSMOS, HDFN, and CDFS fields, respectively, on the assumption of a SMC-like attenuation curve, while open brown objects are those with the Calzetti curve. An open blue square represents the 3σ upper limit of stacked LAEs at $z \sim 2$ with IR observations in Kusakabe et al. (2015, hereafter HK15). (Color online)

In order to compare IRX s and stellar masses of LAEs with the consensus relation, we convert the A_{1600} of our LAEs obtained above to IRX s using equation (1) in Overzier et al. (2011)¹⁰. We find that our LAEs are located near an extrapolation of the consensus relation. Their IRX values are also consistent with that ($\lesssim 2.0$ (3σ)) of typical LAEs obtained by Kusakabe et al. (2015) who constrain the upper limit of the IR luminosity from stacked Spitzer/MIPS $24 \mu\text{m}$ images¹¹. While unlikely, if our LAEs favor the Calzetti attenuation curve, they would be dusty galaxies whose IRX s are more than 10 times higher than expected from the extrapolated consensus relation and comparable to those of 10 times more massive average galaxies.

4.4.2 M_* – SFR Relation

The mode of star formation in star-forming galaxies can be divided into two: the main-sequence (MS) mode where galaxies form stars at moderate rates, making a well-defined sequence in the SFR – M_* plane (SFMS), and the burst mode where galaxies have much higher $sSFR$ s ($= SFR/M_*$) than MS galaxies with similar masses. While it is well established that LAEs are mostly low-mass galaxies, which mode they typically have is still under some debate because of differences in SFR esti-

¹⁰ We shift the derived IRX s downward by 10% because the L_{IR} of the consensus relation is defined as $L_{\text{IR}} \equiv L_{8\text{--}1000\mu\text{m}}$ instead of $L_{\text{IR}} \equiv L_{3\text{--}1000\mu\text{m}}$.

¹¹ This IRX has also been 10% corrected from the original value in Kusakabe et al. (2015, see our footnote 10).

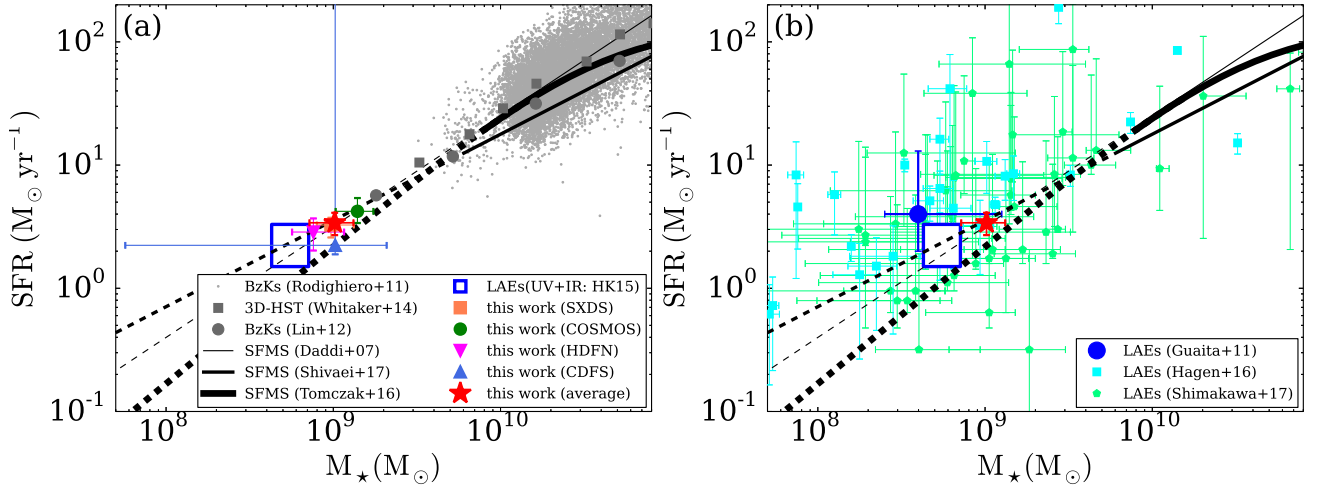


Fig. 8.

SFR plotted against M_* . Panel (a). An orange square, green circle, magenta inverted triangle, and blue triangle represent stacked LAEs with $NB387_{\text{tot}} \leq 25.5$ mag in the SXDS, COSMOS, HDFN, and CDFS fields, respectively, and a red star shows the average over the four fields. The orange square and the red star overlap with each other. A blue open rectangle denotes the permitted range for stacked LAEs from L_{UV} and L_{IR} in Kusakabe et al. (2015). Light gray dots, dim gray squares, and dim gray circles indicate BzKs from Rodighiero et al. (2011), BzKs from Lin et al. (2012), and 3D-HST galaxies from Whitaker et al. (2014), respectively. Black thin middle-width, and thick solid lines represent the star formation main sequence at $z \sim 2$ in Tomczak et al. (2016, hereafter T16), Shivaie et al. (2017, hereafter S17), and Daddi et al. (2007), respectively (determined well using L_{UV} and L_{IR}), with extrapolated parts shown by dashed lines (see also footnote 1). (b) Same as panel (a) but LAEs taken from the literature are also plotted. Cyan squares and light green pentagons show individual LAEs at $z \sim 2$ in Hagen et al. (2016) and Shimakawa et al. (2017), respectively. A blue circle indicates stacked LAEs at $z \sim 2$ in Guaita et al. (2011). SFR s in Hagen et al. (2016) and Shimakawa et al. (2017) are derived from the $IRX - \beta$ relation with the Calzetti curve (Meurer et al. 1999) and SFR s in Guaita et al. (2011) are derived from SED fitting with the Calzetti curve, while SFR s in this work are derived from SED fitting with a SMC-like curve (see also footnote 1). We also show our results with the $IRX - \beta$ and SED fitting with the Calzetti curve in figure 15. (Color online)

mates.

The SFMS itself at $z \sim 2$ has been determined well using rest UV to far-infrared (FIR) data at $M_* \gtrsim 10^{10} M_\odot$ (e.g., Whitaker et al. 2014; Tomczak et al. 2016). Below this stellar mass, the SFMS is suggested to continue at least down to $M_* \sim 10^8 - 10^9 M_\odot$ keeping its power-law slope unchanged (e.g., by Santini et al. 2017, using gravitationally-lensed galaxies in the HST Frontier Fields), although IR data have not been used. In this paper we also simply extrapolate literature SFMS's toward lower masses without changing their power-law slopes.

Figure 8(b) show previous results for LAEs at $z \sim 2 - 2.5$. Hagen et al. (2016) have found that bright individually detected LAEs lie along or above the SFMS, while Shimakawa et al. (2017) have found that fainter, individually detected LAEs lie on the SFMS. Guaita et al. (2010)'s estimates based on stacking analysis have too large errors to distinguish the star formation mode although they are consistent with the MS mode. Kusakabe et al. (2015) have stacked IR and UV images of $z \sim 2$ LAEs to show that they are MS galaxies in average.

The M_* and SFR of our LAEs averaged over the four fields are $M_* = 10.2 \pm 3.0 \times 10^8 M_\odot$ and $SFR = 3.4 \pm 0.7 M_\odot \text{ yr}^{-1}$, respectively. Thus, our LAEs are on average placed near a lower-mass extrapolation of the SFMS as shown by a red star in figure 8(b), confirming the result obtained by Kusakabe et al. (2015) with a 6 times larger survey area using deep IRAC data. We also find in figure 8(a) that the LAEs in individual fields also

lie on the extrapolated SFMS.

Hagen et al. (2016)'s sample is a mixture of two samples: bright spectroscopically-selected LAEs at $z = 1.90 - 2.35$ from the HETDEX survey ($L_{Ly\alpha} > 10^{43} \text{ erg s}^{-1}$; Hagen et al. 2014) and bright NB-selected LAEs at $z \simeq 2.1$ from Guaita et al. (2010) and Vargas et al. (2014) with a counterpart in the 3D-HST catalog. They derive SFR s from the $IRX - \beta$ relation with the Calzetti curve. Note that we also find our LAEs to have higher $sSFR$ s similar to theirs if we use the Calzetti curve as shown in figures 15 (a) – (c)¹². Shimakawa et al. (2017) select LAEs using a narrow-band ($NB \leq 26.55 \text{ mag}$ (5σ)) and only include those with a counterpart in the 3D-HST catalogue (Skelton et al. 2014). They also derive SFR s from the $IRX - \beta$ with the Calzetti curve, while stellar masses are derived from SED fitting without IRAC photometry. Since their LAEs have blue β (~ -1.9 in average), their SFR s do not change so much if a SMC-like curve is used instead. Hashimoto et al. (2017) have also examined six LAEs with $EW_0(Ly\alpha) \simeq 200 - 400 \text{ \AA}$ selected from the same sample as ours and found that they are starburst galaxies with $M_* \sim 10^7 - 10^8 M_\odot$. However, as suggested in Hashimoto et al. (2017), their high $sSFR$ s are probably a consequence of high $EW_0(Ly\alpha)$ s (because younger galaxies

¹²Hagen et al. (2016) suggest either that their LAEs are undergoing starbursts, that the SFMS becomes shallower at low stellar masses and their LAEs are distributed around it, or that their LAEs are biased towards high $Ly\alpha$ luminosities, not representing typical LAEs.

have a larger $EW_0(\text{Ly}\alpha)$ and the stellar population properties of these six LAEs do not represent those of our LAE sample.

We infer that our sample better represents the majority of $z \sim 2$ LAEs because of a wide luminosity coverage ($\sim 0.1 - 2 \times L_{\text{Ly}\alpha}^*$; see Konno et al. 2016) and a simple selection based only on $EW_0(\text{Ly}\alpha) \geq 20-30\text{\AA}$, being less biased toward/against other quantities such as UV luminosity. The majority of $z \sim 2$ LAEs are probably normal star-forming galaxies with low stellar masses in terms of star formation mode.

5 Stellar and Halo Properties

In this section, we combine the stellar masses, $SFRs$, and halo masses derived in the previous sections (summarized in tables 3 and 4) to evaluate two kinds of star formation efficiency in hosting dark halos.

5.1 Relation between M_* and M_h

The stellar to halo mass ratio ($= M_*/M_h$: $SHMR$) indicates the efficiency of star formation in dark halos integrated over time from the onset of star formation until the observed time, which we call integrated SF efficiency. The $SHMR$ as a function of halo mass is known to have a peak over a wide redshift range and the halo mass at the peak (pivot mass) is $\simeq 2 - 3 \times 10^{12} M_\odot$ at $z \sim 2$, although the behavior of the $z \sim 2$ $SHMR$ below $M_h \sim 10^{11} M_\odot$ has not been constrained well (e.g., Behroozi et al. 2013; Moster et al. 2013).

Figure 9(a) shows M_* against M_h for LAEs (Guaita et al. 2010, this study)¹³, star forming galaxies based on clustering analysis (Lin et al. 2012; Ishikawa et al. 2016; Ishikawa 2017)¹⁴, and the average relation based on abundance matching (Behroozi et al. 2013; Moster et al. 2013)¹⁵ at $z \sim 2$. In contrast to Guaita et al.'s result (a blue circle), our LAEs averaged over the four fields lie above a simple lower-mass extrapolation (without changing the slope in the log-log space) of the M_* - M_h relation of star forming galaxies and the average relation. In spite of low halo masses, our LAEs have as a high $SHMR$ of $0.02^{+0.07}_{-0.01}$ as galaxies with the pivot mass, $M_h \simeq 2 - 3 \times 10^{12} M_\odot$ as shown in figure 9(b).

The average relation by Moster et al. (2013) expresses the mean stellar mass of the central galaxy as a function of halo mass and has a double power-law form, while that by Behroozi

et al. (2013) uses the median stellar mass and has five fitting parameters, whose functional form at low halo masses is approximated by a power law¹⁶. Our average stellar mass is a field-average median stellar mass since stellar masses are derived from SED fitting for median-stacked SEDs, which are commonly used to prevent contaminations (see section 4). The field-average mean stellar mass of our sample is possibly higher than the field-average median. In fact, the mean value of K -band flux densities, which is an approximation of stellar mass, is approximately twice as high as the median one in the SXDS field, the field with the deepest K data. We derive effective halo masses of our LAEs from effective biases directly (see section 3.5) assuming a one-to-one correspondence between galaxies and dark matter halos with a narrow range of halo mass. Our field-average effective halo mass probably corresponds to the true mean and/or median within the large uncertainty whose 1σ permitted range is ~ 1 dex. Even though the uncertainty by cosmic variance discussed in section 3.4 is added to the total uncertainty in the field-average halo mass, by which the halo mass and $SHMR$ are written as $M_{h,cv} = 4.0^{+8.4}_{-3.5} \times 10^{10} M_\odot$ and $SHMR = 0.02^{+0.18}_{-0.01}$, respectively, our result is not consistent with the extrapolated average relations within 1σ .

There is of course a possibility that the average relation bends at $\sim 10^{11} M_\odot$ with a much shallower slope and our LAEs are indeed on the relation and thus represent average galaxies. In this case, one must find physical mechanisms causing this sudden bending at such a low mass. In fact, at $z \sim 0$ the slope of the Behroozi et al. (2013) relation becomes slightly shallower below $M_h \sim 10^{11} M_\odot$. Another possibility is that the scatter of the average relation become significantly larger at lower halo masses and the $SHMR$ of our LAEs is within the scatter.

5.2 Baryon Conversion Efficiency

The baryon conversion efficiency (BCE), defined as:

$$BCE = \frac{\dot{M}_*}{\dot{M}_b}, \quad (27)$$

measures the efficiency of star formation in dark halos at the observed time, where \dot{M}_b is the baryon accretion rate (BAR). Here we assume that most of the accreting baryons are in (cold) gas phase (i.e., the BAR is equal to the inflow rate of cold gas). The average BAR at a fixed halo mass is proportional to the halo mass accretion rate, $\dot{M}_h(z, M_h)$, which is estimated as a function of redshift and halo mass from cosmological simulations (Dekel et al. 2009):

$$BAR = f_b \times \dot{M}_h(z, M_h) \quad (28)$$

$$\sim 6 \times \left(\frac{M_h}{10^{12} M_\odot} \right)^{1.15} \times (1+z)^{2.25} M_\odot \text{ yr}^{-1}, \quad (29)$$

¹³ The SFR and stellar mass in Guaita et al. (2010, 2011) are derived from SED fitting to a median-stacked SED and their halo mass is a median halo mass. We plot them without any correction (see also section 3.3).

¹⁴ We recalculate halo masses in Lin et al. (2012) from the effective biases given in their table using the same method as ours.

¹⁵ The values of cosmological parameters adopted in Behroozi et al. (2013) and Moster et al. (2013) are slightly different from ours, but we have not corrected for those differences in this study. The M_h value in Behroozi et al. (2013) becomes ~ 0.15 dex higher at $M_h \leq 10^{12} M_\odot$ when our values are used (P. Behroozi 2017, private communication).

¹⁶ The Behroozi et al. (2013) relations including extrapolated parts in figures 9–11 are taken from the website of P. Behroozi: <http://www.peterbehroozi.com/data.html>. see also footnote 15.

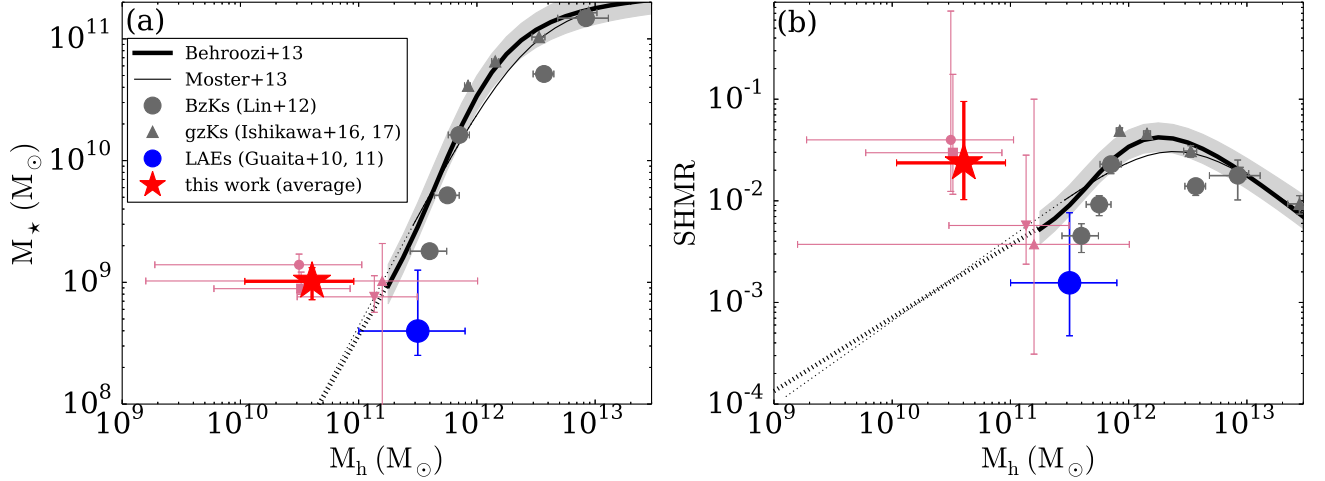


Fig. 9. (a) M_* vs M_h and (b) $SHMR$ vs M_h . For each panel, a filled pink square, circle, inverted triangle, and triangle represent average (stacked) LAEs with $NB387_{\text{tot}} \leq 25.5$ mag in the SXDS, COSMOS, HDFN, and CDFS fields, respectively, and a large red star shows the average over the four fields. A blue circle indicates median (stacked) LAEs at $z \sim 2$ in Guaita et al. (2011). Black thick and thin solid lines represent the average relation of galaxies at $z \sim 2$ in Behroozi et al. (2013) and Moster et al. (2013), respectively; their extrapolations are shown by dotted black lines. A gray shaded region indicates the 1σ uncertainty in M_* in the relation in Behroozi et al. (2013). Gray circles and gray triangles denote BzK galaxies in Lin et al. (2012) and gzK galaxies in Ishikawa et al. (2016) and Ishikawa (2017), respectively. See also footnotes 1 and 13–16. (Color online)

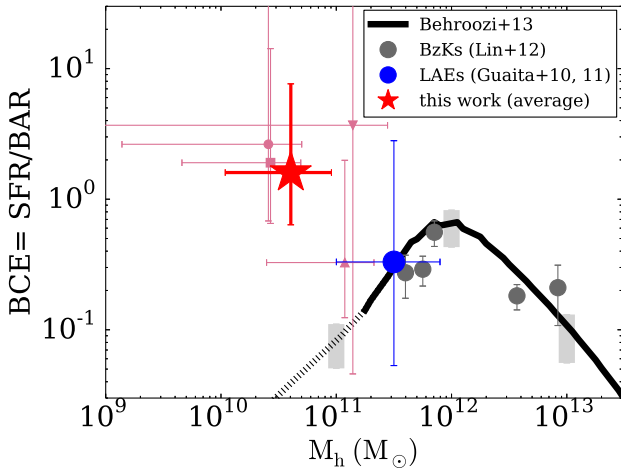


Fig. 10. Baryon conversion efficiency (BCE) as a function of M_h . A filled pink square, circle, inverted triangle, and triangle represent average (stacked) LAEs with $NB387_{\text{tot}} \leq 25.5$ mag in the SXDS, COSMOS, HDFN, and CDFS fields, respectively, and a red star shows the average over the four fields. A blue circle indicates median (stacked) LAEs at $z \sim 2$ in Guaita et al. (2011). A black thick solid and gray circles show the average relation of galaxies at $z \sim 2$ in Behroozi et al. (2013) and measurements for BzK galaxies in Lin et al. (2012), respectively. Extrapolations and 1σ scatters of BCE at fixed M_h are shown by a dotted black line and vertical gray bands, respectively. The scatters of BCE are estimated from scatters of SFR_s at $M_h = 1 \times 10^{11}$, 1×10^{12} , and 1×10^{13} . See also footnotes 1 and 13–16. (Color online)

where $f_b \equiv \Omega_b/\Omega_m = 0.15$.

Figure 10 shows the BCE against halo mass. Guaita et al. (2010, 2011)’s LAEs at $z \sim 2$ have a low or moderate BCE compared with an extrapolation (keeping the slope unchanged) of the average relation by Behroozi et al. (2013) and most of the BzK galaxies in Lin et al. (2012). On the other hand, with $BCE = 1.6^{+6.0}_{-1.0}$, our LAEs lie above the average relation as

shown by a red star. The average relation by Behroozi et al. (2013) expresses the mean SFR as a function of halo mass. Our field-average SFR is derived from SED fitting for median-stacked SEDs and probably does not overestimate the true average SFR , since the median of B -band flux densities, which trace rest-frame UV, is similar to the average B -band flux density. Even when we neglect dust attenuation at UV, $A_{1600} = 0.6 \pm 0.2$ mag, the field-average SFR ($= 3.4 \pm 0.7 \text{ M}_\odot \text{ yr}^{-1}$) decreases only a factor of ~ 2 . Moreover, even when the uncertainty by cosmic variance discussed in section 3.4 is added to the measured value, $BCE = 1.6^{+6.0}_{-1.0}$, the 1σ lower limit of the field-average BCE is still larger than 0.5. Thus, it seems difficult for our LAEs to fall on the average relation shown in figure 10.

As described in section 5.1, logically we cannot rule out the possibilities that our LAEs lie indeed on or near the average relation which changes the slope and/or scatter below $M_h \sim 1 \times 10^{11} \text{ M}_\odot$ for some reason.

6 Discussion

In this section, we obtain a picture of our LAEs in terms of galaxy evolution and discuss the physical origin of their high $SHMR$ and BCE , as well as predicting their present-day descendants. We assume that the three average relations shown in figures 8, 9, and 10 do not change either the slope (in log-log plane) or the scatter at low masses. We also assume that our LAEs are central galaxies. If they are satellite galaxies, their dark matter halo (sub halo) masses will be overestimated and their true $SHMR$ and BCE become higher even more.

6.1 Duty Cycle

The duty cycle of LAEs, $f_{\text{duty}}^{\text{LAEs}}$, is defined as the fraction of dark matter halos hosting LAEs. Previous studies find that $f_{\text{duty}}^{\text{LAEs}}$ at $z \sim 3$ is a few tenths to a few percent (Ouchi et al. 2010; Chiang et al. 2015). We estimate the duty cycle of our LAEs to be:

$$f_{\text{duty}}^{\text{LAEs}} = \frac{ND_{\text{LAE}}}{ND_{\text{DMH}}} \sim 2\%, \quad (30)$$

where ND_{LAE} and ND_{DMH} are the number density of LAEs with $NB_{\text{tot}} \leq 25.5$ mag and that of dark matter halos estimated from the halo mass function at $z \sim 2$ using the calculator provided by Murray et al. (2013), respectively. In this calculation we assume that dark matter halos hosting our LAEs have a one dex range of mass, 10^{10} – $10^{11} M_{\odot}$, since the K -band magnitudes, an approximation of stellar mass, of our LAEs are distributed with an FWHM of ~ 3.2 mag, or ~ 1.3 dex. Our result is comparable with those of previous studies.

We also estimate the fraction of galaxies in a given stellar mass range classified as LAEs (LAE fraction), $f_{\text{gals}}^{\text{LAEs}}$. Assuming that our LAEs have a one dex range of stellar mass, $10^{8.5}$ – $10^{9.5} M_{\odot}$, we obtain:

$$f_{\text{gals}}^{\text{LAEs}} = \frac{ND_{\text{LAE}}}{ND_{\text{gal}}} \sim 10\%, \quad (31)$$

where ND_{gal} is the number density of galaxies estimated by extrapolating Tomczak et al. (2013)'s stellar mass function at $z \sim 2$ – 2.5 below $10^9 M_{\odot}$. This result is comparable with those of previous spectroscopic observations of star forming galaxies at $z \sim 2$ – 2.5 , $\sim 10\%$, in Hathi et al. (2016) and BX galaxies at $z \sim 1.9$ – 2.7 , $\sim 12\%$ in Reddy et al. (2008, with $EW_{\text{Ly}\alpha} \geq 20 \text{ \AA}$). Note that typical galaxies embedded in dark matter halos with $M_{\text{h}} = 10^{10}$ – $10^{11} M_{\odot}$ have lower stellar masses than $M_{\star} = 10^{8.5}$ – $10^{9.5} M_{\odot}$ because of the high $SHMR$ of our LAEs.

The low fractions obtained above imply either that only a few percent of all galaxies can evolve into LAEs and/or that even low-mass galaxies can emit $\text{Ly}\alpha$ only for a very short time.

6.2 Physical Origin of $\text{Ly}\alpha$ Emission

The result that our LAEs have a higher $SHMR$ than average galaxies with the same stellar mass naturally explains why they have strong $\text{Ly}\alpha$ emission. A higher $SHMR$ at a fixed M_{\star} means a lower M_{h} and hence a lower gas mass (M_{gas}), since the M_{gas} of a galaxy is written as $M_{\text{gas}} \simeq f_{\text{b}} M_{\text{h}} - M_{\star}$. Galaxies with a low M_{gas} likely have a low HI column density, thus making it easy for $\text{Ly}\alpha$ photons to escape because of a reduced number of resonant scattering. Indeed, Pardy et al. (2014) have found a tentative anticorrelation of HI gas mass against the $\text{Ly}\alpha$ escape fraction and the $\text{Ly}\alpha$ equivalent width using 14 local galaxies with $\text{Ly}\alpha$ emission ($\text{Ly}\alpha$ Reference Sample; Hayes et al. 2013; Östlin et al. 2014).

Furthermore, with a high BCE , our LAEs may have high

outflow velocities because a high BCE means a high SFR at a fixed M_{h} (recall $\text{BAR} \propto M_{\text{h}}^{1.15}$) and hence a high kinetic energy from star formation at a fixed gravitational binding energy of dark halos. In high-velocity outflowing HI gas, the probability of the resonant scattering of $\text{Ly}\alpha$ photons is reduced because of reduced cross sections of HI atoms due to large relative velocities (e.g., Kunth et al. 1998; Verhamme et al. 2006; Hashimoto et al. 2015).

Note also that our LAEs have absolutely low dust attenuation due probably to a low stellar mass as shown in figure 7, which also helps $\text{Ly}\alpha$ photons survive in galaxies. To summarize, the high $SHMR$, high BCE , and moderate SFR obtained for our LAEs are in concord with the strong $\text{Ly}\alpha$ emission observed.

6.3 Physical Origin of Moderate Star Formation Mode, High $SHMR$, and High BCE

Our LAEs have a higher $SHMR$ and a higher BCE than average galaxies but have a moderate SFR , being located on the (extrapolated) SFMS defined by average galaxies. Indeed, it is not trivial for galaxy formation models to reproduce these three properties simultaneously.

Dutton et al. (2010) have used a semi-analytic model to study the evolution of the SFMS and its dependence on several key parameters in the model. As shown in their figure 12 and our figure 11, model galaxies (at $z \sim 2$) at a fixed halo mass move along the SFMS upward when the super nova (SN) feedback is weakened or the halo's spin parameter is reduced, thus having a higher $SHMR$ and a higher BCE on the SFMS. With a lower feedback efficiency, a more amount of cold gas is stored, giving a higher SFR and a higher stellar mass. A lower spin makes the gas density higher, thereby the star formation efficiency per unit gas mass is elevated. Although these results may not necessarily be applicable to our LAEs whose halo mass is ten times lower, it is interesting to note that there is a relatively simple way to produce MS galaxies with an elevated $SHMR$ and BCE .

It is beyond our scope to identify the mechanism(s) by which our LAEs acquire a high $SHMR$ and a high BCE . If, however, the high $SHMR$ and BCE of our LAEs are due to some systematic differences in one or more parameters controlling the star formation and/or internal structure of halos similar to Dutton et al. (2010)'s study, then it implies that not all but only a certain fraction of (low-mass) halos at $z \sim 2$ experience the LAE phase.

6.4 Present-day Descendants of Our LAEs

LAEs are found to reside in low-mass halos with $M_{\text{h}} \sim 10^{10}$ – $10^{12} M_{\odot}$ over the wide redshift range $z \sim 2$ – 7 as found in section 3.5 (e.g., Ouchi et al. 2005, 2010; Kovač et al. 2007; Gawiser et al. 2007; Shioya et al. 2009; Guaita et al. 2010;

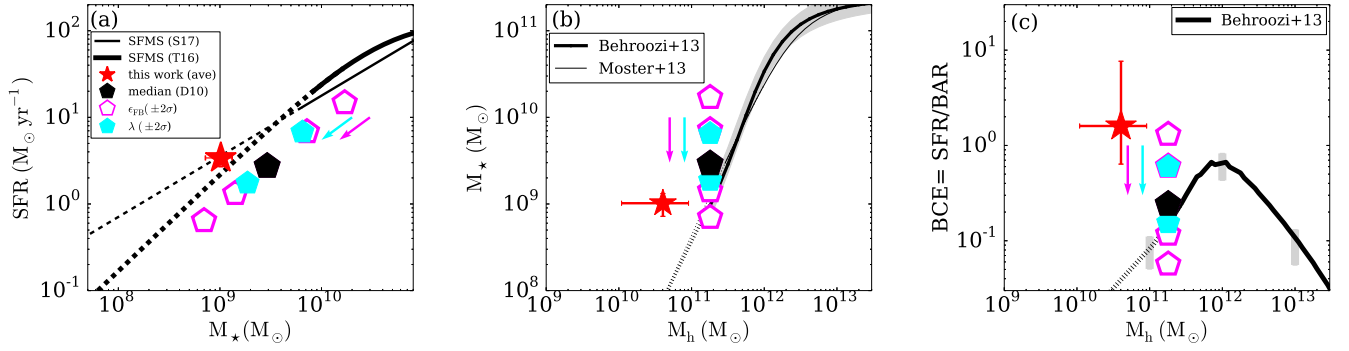


Fig. 11. Changes in the position of model galaxies in the M_* -SFR plane (panel (a)), M_h - M_* plane (panel (b)), and M_h -BCE plane (panel (c)) due to variations in the halo spin parameter, λ , and the feedback efficiency, ϵ_{FB} , calculated by Dutton et al. (2010, hereafter D10). Pentagons show D10s model galaxies with a fixed halo mass ($M_{h, z=0} = 4 \times 10^{11} M_\odot$, corresponding to $\sim 2 \times 10^{11} M_\odot$ at $z = 2$ according to figures 7 and 8 in Behroozi et al. (2013)), where black, cyan, and magenta colors denote, respectively, positions with median halo parameters, those with $\pm 2\sigma$ variation in λ , and those with $\pm 2\sigma$ variation in ϵ_{FB} . All model data of M_* and SFR are taken from figure 12 in D10. The bars of model galaxies are calculated from equation 29. Cyan and magenta arrows indicate the direction in which galaxies move when λ and ϵ_{FB} increase. In all panels, red stars represent the average LAEs with $NB387_{tot} \leq 25.5$ mag. In panel (a), several SFMS measurements in previous studies are shown by black lines in the same manner as figure 8. The average relations in Behroozi et al. (2013) and Moster et al. (2013) are plotted by black lines in panels (b) and (c), similar to figures 9 and 10. See also footnotes 1 and 13–16. (Color online)

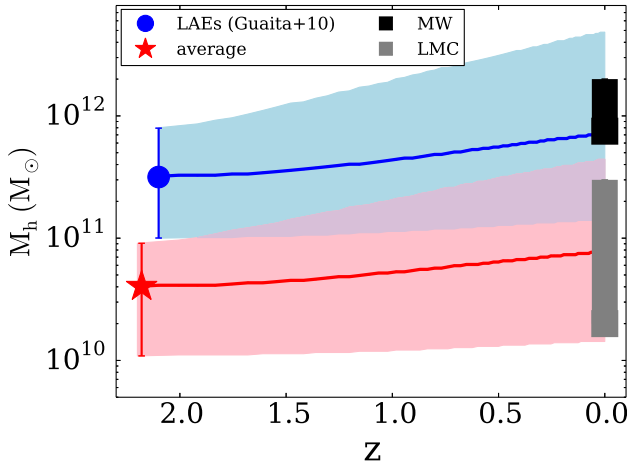


Fig. 12. Dark matter halo mass evolution as a function of redshift predicted by the EPS formalism. A red (blue) curve indicates the evolution of the mode of the M_h distribution starting from the mass of our $z = 2.2$ LAEs shown by a red star (Guaita et al. 2010, 's $z = 2.1$ LAEs shown by a blue circle), with a shaded region indicating the 68% confidence interval of the distribution. Black and gray rectangles represent the measured halo mass ranges of the MW and the LMC, respectively (e.g., Wilkinson & Evans 1999; Kafle et al. 2014; van der Marel & Kallivayalil 2014; Eadie et al. 2015; Peñarrubia et al. 2016, see also Wang et al. 2015).

Bielby et al. 2016; Diener et al. 2017; Ouchi et al. 2017). In other words, the bias value of LAEs tends to decrease with decreasing redshift more rapidly than that of dark matter halos (see figure 7 in Ouchi et al. 2017). This trend, although perhaps biased because faint LAEs in lower-mass halos are missed at high redshifts, implies that at lower redshifts, only galaxies with relatively lower masses in the halo mass function can be LAEs, which is analogous to and/or maybe related to downsizing (Cowie et al. 1996).

The roughly constant halo mass against redshift also implies that local descendants of LAEs vary depending on their red-

shift. The growth of dark matter halos is statistically predicted by the extended Press-Schechter (EPS; Press & Schechter 1974; Bond et al. 1991; Bower 1991) model. A detailed description of the EPS model can be found in Hamana et al. (2006, and the references therein).

Previous studies suggest that LAEs at $z \sim 4-7$ evolve into massive elliptical galaxies at $z = 0$ (Ouchi et al. 2005; Kovač et al. 2007; Ouchi et al. 2010), while LAEs at $z \sim 3$ are expected to be progenitors of present-day L_* galaxies (Gawiser et al. 2007; Ouchi et al. 2010). Guaita et al. (2010) show that LAEs at $z \sim 2$ could be progenitors of present-day L_* galaxies like the Milky Way (MW) and that they could also be descendants of $z \sim 3$ LAEs, depending on star formation and dust formation histories (see also Acquaviva et al. 2012).

With the EPS model¹⁷, we find that at $z = 0$ our LAEs are embedded in dark matter halos with a median mass similar to the mass of the Large Magellanic Cloud (LMC: $M_h \sim 0.2-3 \times 10^{11} M_\odot$; van der Marel & Kallivayalil 2014; Peñarrubia et al. 2016, and references therein), not in MW-like halos ($M_h \sim 8 \times 10^{11}-2 \times 10^{12} M_\odot$; e.g., Wilkinson & Evans 1999; Kafle et al. 2014; Eadie et al. 2015, summarized in figure 1 in Wang et al. 2015), as shown in figure 12.

This is consistent with the prediction by Acquaviva et al. (2012) from SED fitting that LAEs at $z \sim 3$, which are progenitors of present-day L_* galaxies, do not evolve into LAEs at $z \sim 2$. Combined with the previous studies, our result implies that the mass of present-day descendants of halos hosting LAEs depends on the redshift at which they are observed, with higher- z LAEs evolving into more massive halos.

Since the stellar mass of our LAEs, $10.2 \pm 3.0 \times 10^8 M_\odot$, is comparable to that of the LMC within only a factor of ~ 3

¹⁷We use a publicly released code by T. Hamana: <http://th.nao.ac.jp/MEMBER/hamanatk/OPENPRO/index.html>.

($M_* \sim 2.9 \times 10^9 M_\odot$: van der Marel et al. 2002), their star-formation has to be largely suppressed over most of the cosmic time until $z = 0$, or even be quenched, if they really become LMC-like galaxies. The star formation history of the LMC has been inferred to have multiple components, i.e., an initial burst and subsequent periods with moderate or quiescent star formation (e.g., Harris & Zaritsky 2009). For example, Rezaei Kh. et al. (2014) argue that it consists of two components: an initial burst of ~ 10 Gyr ago, or at $z \sim 2$, with a $SFR \sim 2.4 M_\odot \text{ yr}^{-1}$ assembling $\sim 90\%$ of the total mass, and a much milder star formation with $SFR \sim 0.3 M_\odot \text{ yr}^{-1}$ after that as shown in their figure 4. Although Weisz et al. (2013) estimate that the initial star formation until $z \sim 2$ is more moderate with $SFR \sim 0.3 M_\odot \text{ yr}^{-1}$, most of the previous studies have a common view of unsustainable star formation. If our LAEs follow such a history with suppressed star formation over $\sim 5 - 10 \times 10^9$ Gyr, they will grow up to be LMC-like galaxies at $z = 0$ with an $SHMR$ consistent with the average relation and a moderate $sSFR$.

6.5 Future Survey

In the near future, we will extend this work using new $NB387$ data from $\simeq 25 \text{ deg}^2$ taken with Hyper Suprime-Cam as part of a large imaging survey program (Aihara et al. 2017). This program uses five broadband and four NB filters, among which the new $NB387$ is included. We call the LAE surveys with the four NB filters SILVERRUSH (Ouchi et al. 2017; Shibuya et al. 2017a). The survey volume for $NB387$ ($z \sim 2$) LAEs is $6 \times 10^6 (h_{100}^{-1} \text{ Mpc})^3$ with an expected number of ~ 9000 objects. As shown in figures 5(a) and 5(b), the uncertainty from cosmic variance is expected to be negligibly small, $\sim 3\%$, compared with other uncertainties. With the HSC data, we will be able to determine the $SHMR$ and BCE of $z \sim 2$ LAEs without suffering from cosmic variance.

7 Conclusions

We have investigated stellar populations and halo masses of LAEs at $z \sim 2$, low-mass galaxies at cosmic noon, using ~ 1250 $NB387$ -selected LAEs from four separate fields with $\sim 1 \text{ deg}^2$ in total. In particular, we have derived the average SF mode, $SHMR$, and BCE of objects with $NB387 \leq 25.5$ for which measurements for all four fields are available, and discussed star formation activity and its dependence on halo mass. Our main results are as follows.

1. The bias parameter of $NB387 \leq 25.5$ objects averaged over the four fields is $b_{g, \text{eff}}^{\text{ave}} = 1.22_{-0.18}^{+0.16}$, which is lower than that in Guaita et al. (2010) from 0.3 deg^2 with a probability of 96%. We estimate an external error from cosmic variance which inversely scales with the square root of the survey

area. The high bias value obtained by Guaita et al. (2010) becomes consistent with our value if the uncertainties from cosmic variance, $\pm 26\%$ and $\pm 51\%$ for this work and Guaita et al. (2010), are considered. We have also found that b does not significantly change with limiting $NB387$ magnitude, or limiting $\text{Ly}\alpha$ luminosity, which may be partly due to two trends canceling out with each other: galaxies in more massive halos have brighter intrinsic $\text{Ly}\alpha$ luminosities but lower $\text{Ly}\alpha$ escape fractions.

2. The halo mass corresponding to the above $b_{g, \text{eff}}^{\text{ave}}$ value is $4.0_{-2.9}^{+5.1} \times 10^{10} M_\odot$. This value is roughly comparable to previous measurements for $z \sim 3 - 7$ LAEs with similar $\text{Ly}\alpha$ luminosities, $M_h \sim 10^{10} - 10^{12} M_\odot$ (e.g., Ouchi et al. 2010), suggesting that the mass of dark halos which can host typical LAEs is roughly unchanged with time.
3. The mean of each stellar parameter over the four fields is: $M_* = 10.2 \pm 3.0 \times 10^8 M_\odot$, $A_{1600} = 0.6 \pm 0.2 \text{ mag}$, $\text{Age} = 3.8 \pm 0.6 \times 10^8 \text{ yr}$, and $\text{SFR} = 3.4 \pm 0.7 M_\odot \text{ yr}^{-1}$. Our LAEs are thus located near an extrapolation of the consensus relation of IRX against stellar mass with an assumption of a SMC-like attenuation curve (see figure 7). We have also found that our LAEs are on average placed near a lower-mass extrapolation of the SFMS, confirming the results obtained by Kusakabe et al. (2015) with a ~ 6 times larger survey area (shown in figure 8).
4. With $SMHR = 0.02_{-0.01}^{+0.07}$, our LAEs lie above a simple lower-mass extrapolation of the average $M_* - M_h$ relation (figure 9). The higher $SHMR$ than average galaxies with the same M_* may make it easy for $\text{Ly}\alpha$ photons to escape since they are expected to have lower gas masses (baryon mass) and thus lower HI column densities. Our LAEs also have a high $BCE = 1.6_{-1.0}^{+6.0}$, lying above the average $BCE - M_h$ relation (figure 10). Thus, our LAEs have been converting baryons into stars more efficiently than average galaxies with similar M_h both in the past and at the observed epoch but with a moderate SF similar to average galaxies. Galaxies with weak SN feedback and small halo's spin parameters possibly have such properties according to the semi-analytic model by Dutton et al. (2010).
5. The duty cycle of LAEs (fraction of $M_h \sim 3 \times 10^{10} M_\odot$ halos hosting LAEs) is estimated to be $\sim 2\%$, and the LAE fraction (fraction of $M_* \sim 1 \times 10^9 M_\odot$ galaxies classified as LAEs) is found to be $\sim 10\%$. These low fractions imply either that only a small fraction of all galaxies can evolve into LAEs and/or that even low-mass galaxies can emit $\text{Ly}\alpha$ only for a very short time.
6. We have calculated the halo mass evolution of our LAEs with the EPS model, to find that at $z = 0$ our LAEs are embedded in dark matter halos with a median halo mass similar to the mass of the Large Magellanic Cloud (LMC). If their star-formation is largely suppressed after the observed time

until $z = 0$ similar to the star-formation history of the LMC, they would have a similar *SHMR* to the present-day LMC. This result, combined with the previous studies, implies that the mass of present-day descendant halos of LAEs depends on the redshift at which the LAEs are observed, with higher- z LAEs evolving into more massive halos.

Acknowledgments

We are grateful to Lihwai Lin and Li-Ting Hsu for kindly providing us with J , H and K_s images of the HDFN field and data in Lin et al. (2012) plotted in figures 8, 9 and 10. We are also grateful to Yoshiaki Ono for giving insightful comments and suggestions on SED fitting. We would like to show our appreciation to Takashi Hamana for helpful comments on cosmic variance and computer programs of the covariance of dark matter angular correlation function and the EPS model. We would like to express our gratitude to David Sobral, Naveen A. Reddy, Giulia Rodighiero, and Shogo Ishikawa for kindly providing their data plotted in figures 5(a), 7, 8, and 9, respectively. We would like to thank Alex Hagen, James E. Rhoads, Jorrit Matthee, and Peter S. Behroozi for useful comments on their results. We also would like to thank Akio K. Inoue, Cai-Na Hao, Hidenobu Yajima, Ikkoh Shimizu, Ken Mawatari, Kotaro Kohno, Kyoung-Soo Lee and Tsutomu T. Takeuchi for insightful discussion. We acknowledge Ryota Kawamata, Taku Okamura, and Kazushi Irikura for constructive discussions at weekly meetings. This work is based on observations taken by the Subaru Telescope which is operated by the National Astronomical Observatory of Japan. The authors wish to recognize and acknowledge the very significant cultural role and reverence that the summit of Maunakea has always had within the indigenous Hawaiian community. This research made use of IRAF, which is distributed by NOAO, which is operated by AURA under a cooperative agreement with the National Science Foundation and of Python packages for Astronomy: Astropy (The Astropy Collaboration et al. 2013), Colossus, CosmoloPy and PyRAF, which is produced by the Space Telescope Science Institute, which is operated by AURA for NASA. H.K acknowledges support from the JSPS through the JSPS Research Fellowship for Young Scientists.

Appendix 1 Result of SED fitting with different assumptions

We show the SED fitting results with the Calzetti curve and without nebular emission below.

A.1.1 The Calzetti Curve

We also examine the cases of the Calzetti curve for comparison. The best-fit parameters with a SMC-like curve and the Calzetti curve are listed in table 5. Figures 6 and 13 show the best-fit SEDs with the observed ones in the case with a SMC-like curve and the Calzetti curve, respectively. We compare the best-fit parameters in subsection 4.4.

A.1.2 Without nebular emission

It is well known that considering nebular emission generally leads to a lower stellar mass (e.g., de Barros et al. 2014). To obtain upper limits of stellar mass and determine the star formation mode of our LAEs, we also examine the case without nebular emission, $f_{\text{esc}}^{\text{ion}} = 1$. The best-fit parameters with a SMC-like curve and the Calzetti curve are listed in table 6. Figure 6 shows the best-fit SEDs with the observed ones in the case with a SMC-like curve and the Calzetti curve.

When we assume a SMC-like curve, the average stellar mass and SFR without nebular emission, $M_{\star} = 11.2 \pm 2.2 \times 10^8 M_{\odot}$ and $SFR = 3.2 \pm 1.0 M_{\odot} \text{ yr}^{-1}$, are consistent with those with nebular emission, $M_{\star} = 10.2 \pm 3.0 \times 10^8 M_{\odot}$ and $SFR = 3.4 \pm 0.7 M_{\odot} \text{ yr}^{-1}$. This means that the average stellar mass and star formation mode of our LAEs are insensitive to $f_{\text{esc}}^{\text{ion}}$ when a SMC-like curve is used. On the other hand, if we assume the Calzetti curve, the average SFR without nebular emission, $SFR = 51.8 \pm 7.8 M_{\odot} \text{ yr}^{-1}$, is higher than that with nebular emission, $SFR = 12.7 \pm 1.0 M_{\odot} \text{ yr}^{-1}$ although their average stellar masses are consistent, $M_{\star} = 4.7 \pm 0.7 \times 10^8 M_{\odot}$ and $M_{\star} = 3.4 \pm 0.8 \times 10^8 M_{\odot}$. With this high SFR, our LAEs lie above the SFMS at $z \sim 2$. However, this case seems unrealistic because our LAEs have Ly α emission, one of nebular emission lines. Indeed, the reduced χ square values in the case without nebular emission are larger than those with nebular emission in all the fields except SXDS. In addition, results with $f_{\text{esc}}^{\text{ion}} = 1$ give a high UV attenuation of $A_{1600} = 2.9 \pm 0.3$ mag and hence a high IRX ($= 21_{-5}^{+7}$), which is significantly higher than predicted by the consensus relation (see figure 7).

Appendix 2 SFMS based on the IRX - β relation with the Calzetti curve

In the discussion of the star formation mode of LAEs at $z \sim 2$ in section 4.4.2, we derive the average SFR of our LAEs using SED fitting with a SMC-like curve, while Hagen et al. (2016) and Shimakawa et al. (2017) derive SFRs using the $IRX - \beta$ relation with the Calzetti curve. For a fair comparison, figure 15(c) shows our results with the $IRX - \beta$ relation with the Calzetti curve (Meurer et al. 1999). We find our LAEs to have higher sSFRs similar to LAEs in Hagen et al. (2016). Note that the selections of these three samples are different as described

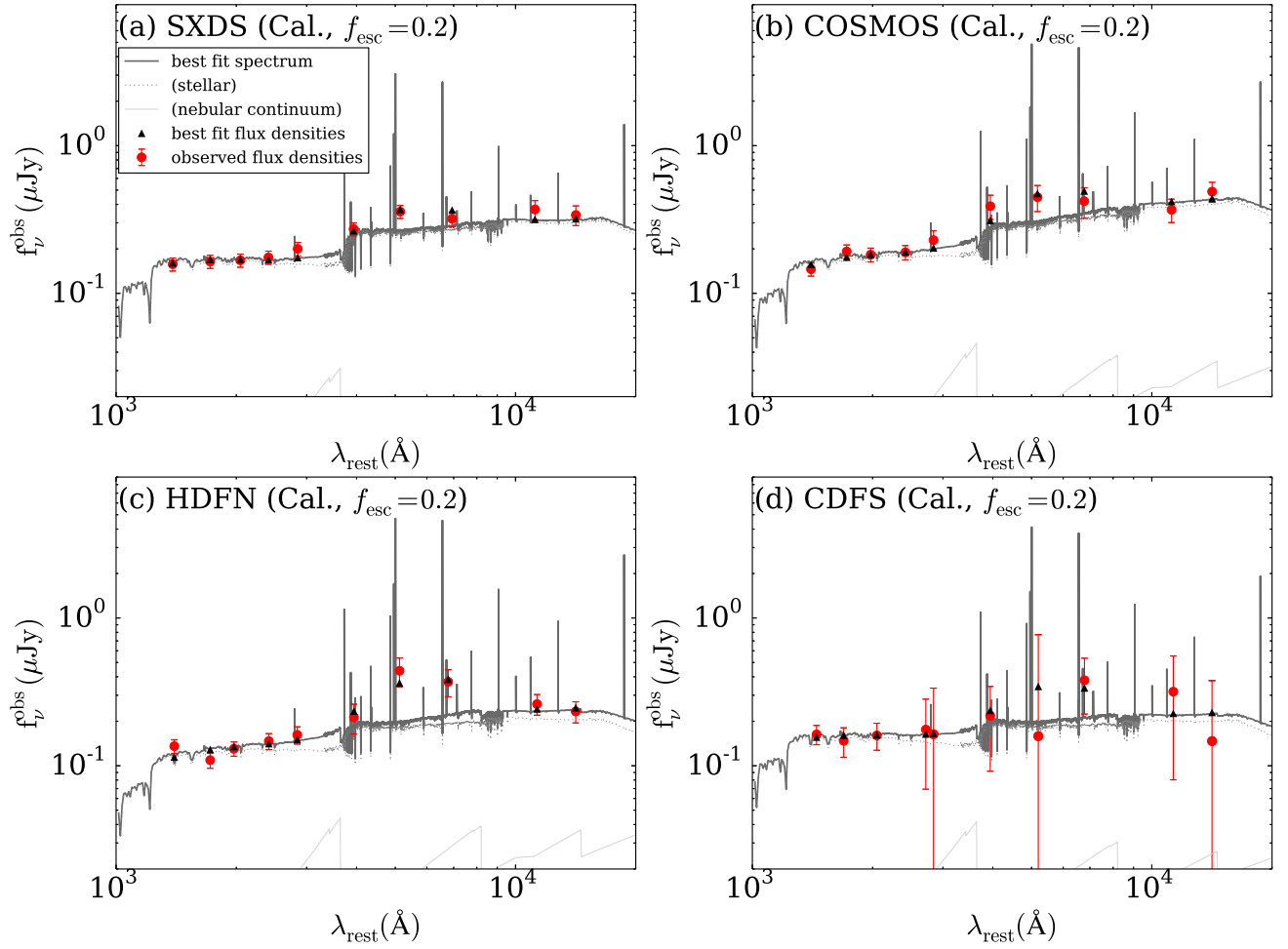


Fig. 13. Same as figure 6 but with the Calzetti curve. Panels (a) to (d) show results for SXDS, COSMOS, HDFN, and CDFS, respectively. (Color online)

in section 4.4.2. We also compare our results by the three different methods discussed in appendix 1.1 and in this section (see figures 15(a) and (b)).

Table 5. Results of SED fitting with a SMC-like curve and the Calzetti curve $(f_{\text{esc}}^{\text{ion}} = 0.2)$.

attenuation curve	M_{\star} ($10^8 M_{\odot}$)	$E(B-V)_{\star} [A_{1600}]$ (mag)	Age (10^8 yr)	SFR ($M_{\odot} \text{yr}^{-1}$)	χ_r^2
	(1)	(2)	(3)	(4)	(5)
SXDS					
SMC	$9.7^{+3.6}_{-1.7}$	$0.05^{+0.01}_{-0.02} [0.6^{+0.1}_{-0.2}]$	$3.6^{+2.8}_{-1.1}$	$3.3^{+0.5}_{-0.7}$	0.604
Calzetti	$7.8^{+3.4}_{-1.9}$	$0.11^{+0.02}_{-0.05} [1.1^{+0.2}_{-0.5}]$	$1.6^{+2.4}_{-0.7}$	$5.7^{+1.7}_{-2.3}$	0.665
COSMOS					
SMC	$14.0^{+3.4}_{-3.6}$	$0.07^{+0.02}_{-0.02} [0.8^{+0.2}_{-0.2}]$	$4.1^{+2.4}_{-1.8}$	$4.2^{+1.2}_{-0.8}$	0.473
Calzetti	$7.9^{+5.1}_{-2.5}$	$0.18^{+0.03}_{-0.05} [1.8^{+0.3}_{-0.5}]$	$0.7^{+1.6}_{-0.4}$	$12.3^{+6.4}_{-5.5}$	0.648
HDFN					
SMC	$7.6^{+4.0}_{-1.9}$	$0.06^{+0.02}_{-0.03} [0.7^{+0.2}_{-0.4}]$	$3.2^{+4.0}_{-1.4}$	$2.9^{+0.8}_{-0.8}$	1.298
Calzetti	$3.2^{+0.6}_{-0.8}$	$0.20^{+0.02}_{-0.03} [2.0^{+0.2}_{-0.3}]$	$0.3^{+0.2}_{-0.1}$	$13.3^{+5.1}_{-3.9}$	0.866
CDFS					
SMC	$10.3^{+11.1}_{-9.7}$	$0.02^{+0.07}_{-0.01} [0.2^{+0.8}_{-0.1}]$	$5.7^{+8.6}_{-5.7}$	$2.2^{+53.4}_{-0.4}$	0.120
Calzetti	$3.1^{+17.5}_{-2.4}$	$0.14^{+0.05}_{-0.13} [1.4^{+0.5}_{-1.3}]$	$0.4^{+14.0}_{-0.3}$	$9.0^{+23.4}_{-7.1}$	0.101
Average					
SMC	10.2 ± 3.0	$0.06 \pm 0.02 [0.6 \pm 0.2]$	3.8 ± 0.6	3.4 ± 0.7	
Calzetti	3.4 ± 0.8	$0.19 \pm 0.01 [1.9 \pm 0.1]$	0.3 ± 0.06	12.7 ± 1.0	

Note. (1) The best fit stellar mass; (2) the best-fit color excess [UV attenuation]; (3) the best fit age; (4) the best fit SFR; (5) reduced chi-squared value. The UV attenuation is derived from the attenuation curve listed in the first column. Metallicity, redshift, and $f_{\text{esc}}^{\text{ion}}$ are fixed to $0.2Z_{\odot}$, 2.18, and 0.2, respectively.

Table 6. Results of SED fitting without nebular emission, $f_{\text{esc}}^{\text{ion}} = 1$.

attenuation curve	M_{\star} ($10^8 M_{\odot}$)	$E(B-V)_{\star} [A_{1600}]$ (mag)	Age (10^8 yr)	SFR ($M_{\odot} \text{yr}^{-1}$)	χ_r^2
	(1)	(2)	(3)	(4)	(5)
SXDS					
SMC	$11.4^{+2.7}_{-1.3}$	$0.06^{+0.02}_{-0.02} [0.7^{+0.2}_{-0.2}]$	$3.6^{+2.1}_{-1.1}$	$3.9^{+0.9}_{-0.8}$	0.350
Calzetti	$5.1^{+7.1}_{-0.4}$	$0.27^{+0.02}_{-0.16} [2.7^{+0.2}_{-1.6}]$	$0.1^{+2.4}_{-0.0}$	$45.3^{+12.0}_{-40.0}$	0.586
COSMOS					
SMC	$14.6^{+5.2}_{-2.7}$	$0.08^{+0.02}_{-0.02} [1.0^{+0.2}_{-0.2}]$	$3.6^{+2.8}_{-1.3}$	$4.9^{+1.3}_{-1.1}$	0.611
Calzetti	$6.6^{+1.5}_{-0.7}$	$0.29^{+0.01}_{-0.04} [2.9^{+0.1}_{-0.4}]$	$0.1^{+0.2}_{-0.0}$	$56.2^{+12.8}_{-26.4}$	0.821
HDFN					
SMC	$9.8^{+2.4}_{-2.5}$	$0.05^{+0.03}_{-0.02} [0.6^{+0.4}_{-0.2}]$	$4.5^{+2.7}_{-2.0}$	$2.7^{+1.0}_{-0.5}$	1.865
Calzetti	$4.4^{+0.0}_{-0.8}$	$0.30^{+0.00}_{-0.04} [3.0^{+0.0}_{-0.4}]$	$0.09^{+0.03}_{-0.01}$	$51.8^{+5.9}_{-18.9}$	1.653
CDFS					
SMC	$13.1^{+10.9}_{-8.9}$	$0.02^{+0.06}_{-0.01} [0.2^{+0.7}_{-0.1}]$	$7.1^{+8.9}_{-6.2}$	$2.3^{+3.0}_{-0.3}$	0.148
Calzetti	$12.1^{+12.7}_{-10.0}$	$0.05^{+0.25}_{-0.04} [0.5^{+2.5}_{-0.4}]$	$5.1^{+11.9}_{-5.1}$	$2.9^{+135.8}_{-1.0}$	0.157
Average					
SMC	11.2 ± 2.2	$0.06 \pm 0.02 [0.6 \pm 0.2]$	4.1 ± 0.8	3.2 ± 1.0	
Calzetti	4.7 ± 0.7	$0.29 \pm 0.03 [2.9 \pm 0.3]$	0.09 ± 0.01	51.8 ± 7.8	

Note. (1) The best fit stellar mass; (2) the best-fit color excess [UV attenuation]; (3) the best fit age; (4) the best fit SFR; (5) reduced chi-squared value. The UV attenuation is derived from the attenuation curve listed in the first column. Metallicity, redshift, and $f_{\text{esc}}^{\text{ion}}$ are fixed to $0.2Z_{\odot}$, 2.18, and 1, respectively.

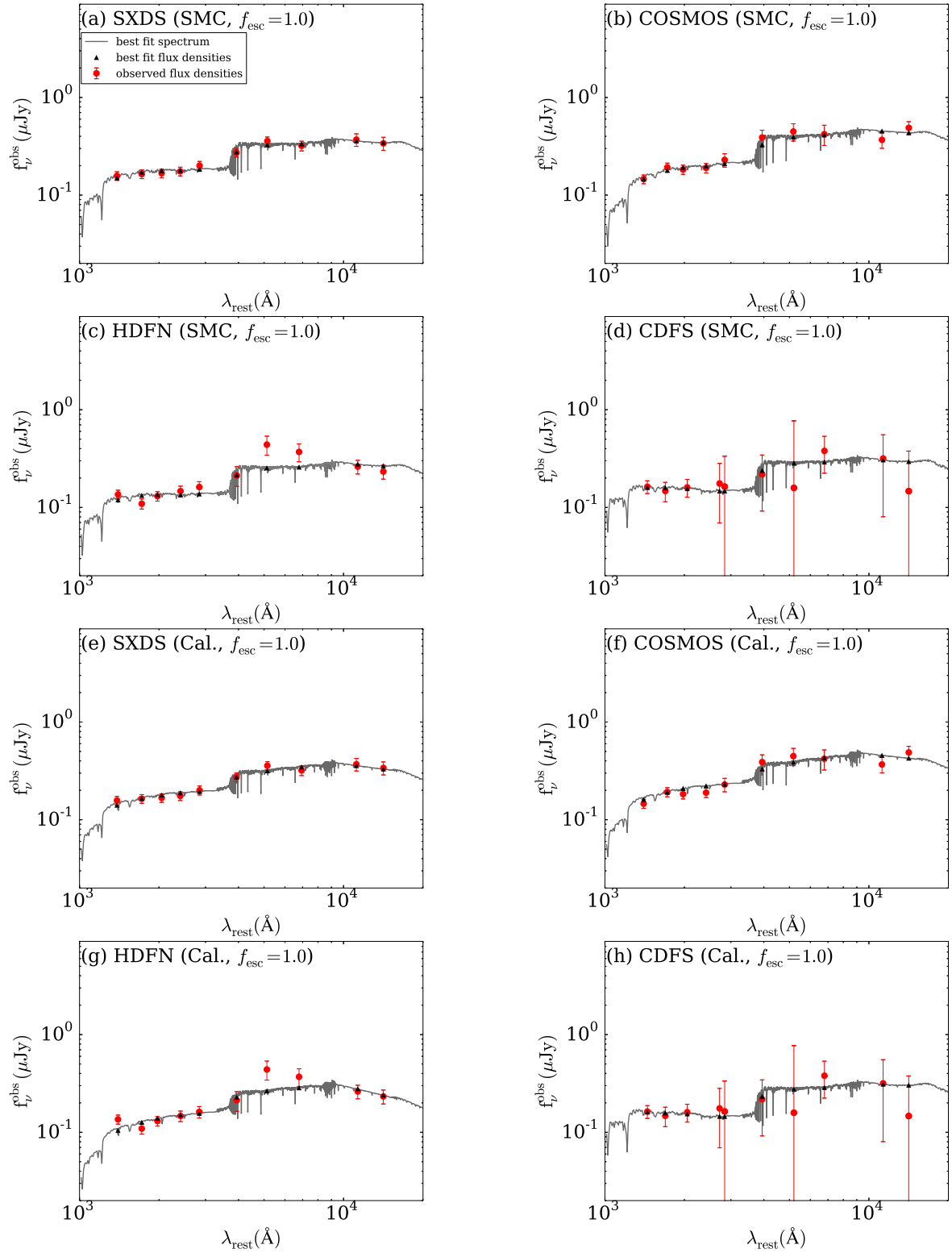
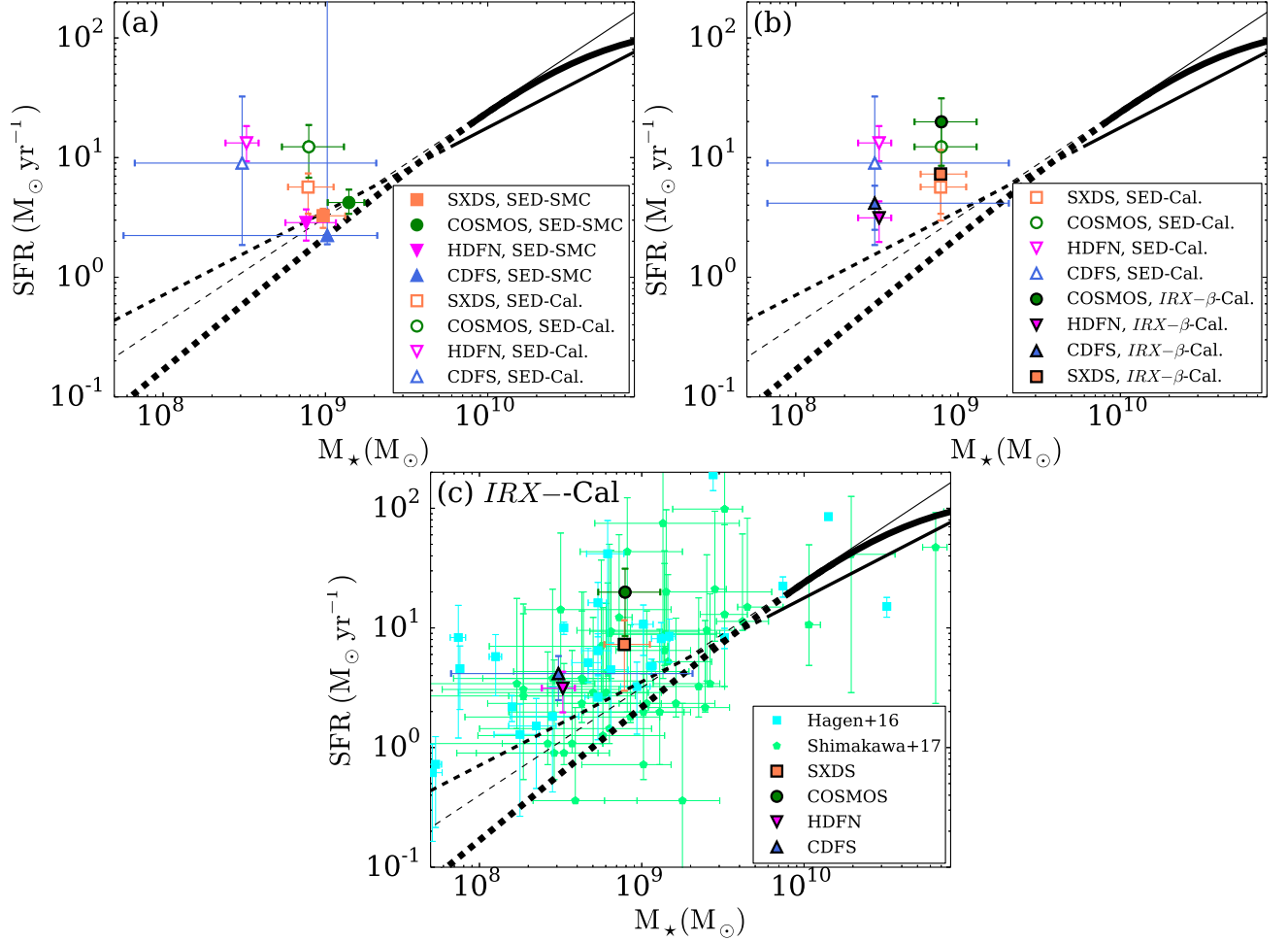


Fig. 14. Same as figure 6 but without nebular emission, $f_{\text{esc}}^{\text{ion}} = 1$. Panels (a) to (d) show results with a SMC-like curve for SXDS, COSMOS, HDFN, and CDFS, respectively. Panels (e) to (h) show results with the Calzetti curve for SXDS, COSMOS, HDFN, and CDFS, respectively. (Color online)

**Fig. 15.**

SFR plotted against M_{\star} . Panels (a) and (b) compare different SFR calculation methods for our LAEs; in panel (a) $SFRs$ calculated from SED fitting with two different attenuation curves are compared; in panel (b) $SFRs$ from SED fitting are compared with those from the $IRX - \beta$ relation, where the Calzetti curve is used in both calculations. Panel (c) uses the $IRX - \beta$ relation with the Calzetti curve and compares our LAEs with Hagen et al. (2016)'s and Shimakawa et al. (2017)'s. In panel (a), orange squares, green circles, magenta inverted triangles, and blue triangles represent stacked LAEs with $NB387_{\text{tot}} \leq 25.5$ mag in the SXDS, COSMOS, HDFN, and CDFS fields, respectively; filled and open symbols are for a SMC-like curve and the Calzetti curve, respectively. In panel (b), encircled symbols indicate that $SFRs$ are derived from the $IRX - \beta$ relation with the Calzetti curve (Meurer et al. 1999). In panel (c), cyan squares and light green pentagons show individual LAEs at $z \sim 2$ in Hagen et al. (2016) and Shimakawa et al. (2017), respectively; in both studies, $SFRs$ are derived from the $IRX - \beta$ relation with the Calzetti curve (Meurer et al. 1999). Our results based on the $IRX - \beta$ relation with the Calzetti curve are also plotted (encircled symbols). In all panels, several SFMS measurements in previous studies are shown by black lines in the same manner as figure 8. See also footnote 1. (Color online)

References

- Acquaviva, V., Vargas, C., Gawiser, E., & Guaita, L. 2012, *The Astrophysical Journal*, 751, L26
- Aihara, H., Arimoto, N., Ouchi, M., et al. 2017, *ArXiv*, 1704.07455, 1
- Ashby, M. L. N., Willner, S. P., Fazio, G. G., et al. 2013, *The Astrophysical Journal*, 769, 80
- Behroozi, P. S., Wechsler, R. H., & Conroy, C. 2013, *The Astrophysical Journal*, 770, 57
- Bielby, R. M., Tummuangpak, P., Shanks, T., et al. 2016, *Monthly Notices of the Royal Astronomical Society*, 456, 4061
- Blanc, G. a., Adams, J. J., Gebhardt, K., et al. 2011, *The Astrophysical Journal*, 736, 31
- Bond, J. R., Cole, S., Efstathiou, G., & Kaiser, N. 1991, *The Astrophysical Journal*, 379, 440
- Bouwens, R. J., Aravena, M., Decarli, R., et al. 2016, *The Astrophysical Journal*, 833, 72
- Bower, R. G. 1991, *MNRAS*, 248, 332
- Brocklehurst, M. 1971, *MNRAS*, 153, 471
- Bruzual, G., & Charlot, S. 2003, *Monthly Notices of the Royal Astronomical Society*, 344, 1000
- Calzetti, D., Armus, L., Bohkin, R., et al. 2000, *ApJ*, 533, 682
- Capak, P., Cowie, L. L., Hu, E. M., et al. 2004, *The Astronomical Journal*, 127, 180
- Capak, P., Aussel, H., Ajiki, M., et al. 2007, *The Astrophysical Journal Supplement Series*, 172, 99
- Cardamone, C. N., van Dokkum, P. G., Urry, C. M., et al. 2010, *The Astrophysical Journal Supplement Series*, 189, 270
- Chabrier, G., & Chabrier, G. 2003, *PASP*, 115, 763
- Chiang, Y.-K., Overzier, R. A., Gebhardt, K., et al. 2015, *The Astrophysical Journal*, 808, 37
- Ciardullo, R., Gronwall, C., Wolf, C., et al. 2012, *The Astrophysical Journal*, 744, 110
- Cochrane, R. K., Best, P. N., Sobral, D., et al. 2017, *MNRAS*, 469, 2913
- Cohn, J. D. 2009, *arXiv*, 0503285v3, doi:10.1016/j.newast.2005.08.002
- Cowie, L. L., Barger, A. J., & Hu, E. M. 2010, *The Astrophysical Journal*, 711, 928
- Cowie, L. L., Songaila, A., Hu, E. M., & Cohen, J. G. 1996, *The Annals of Statistics*, 112, 839
- Curtis-Lake, E., McLure, R. J., Pearce, H. J., et al. 2012, *Monthly Notices of the Royal Astronomical Society*, 422, 1425
- Daddi, E., Dickinson, M., Morrison, G., et al. 2007, *ApJ*, 670, 156
- Damen, M., Labbé, I., van Dokkum, P. G., et al. 2011, *The Astrophysical Journal*, 727, 1
- de Barros, S., Schaerer, D., & Stark, D. P. 2014, *Astronomy & Astrophysics*, 563, A81
- Dekel, A., Birnboim, Y., Engel, G., et al. 2009, *ArXiv e-prints*, ArXiv:0808, 1
- Diemer, B., & Kravtsov, A. V. 2015, *The Astrophysical Journal*, 799, 108
- Diener, C., Wisotzki, L., Schmidt, K. B., et al. 2017, 7, 1
- Dressler, A., Martin, C. L., Henry, A., Sawicki, M., & McCarthy, P. 2011, *ApJ*, 71, doi:10.1088/0004-637X/740/2/71
- Dutton, A. A., van den Bosch, F. C., & Dekel, A. 2010, *Monthly Notices of the Royal Astronomical Society*, 405, 1690
- Eadie, G. M., Harris, W. E., & Widrow, L. M. 2015, *The Astrophysical Journal*, 806, 54
- Eisenstein, D. J., & Hu, W. 1998, *The Astrophysical Journal*, 496, 605
- . 1999, *the Astrophysical Journal*, 511, 5
- Erb, D. K., Steidel, C. C., Shapley, A. E., et al. 2006, *The Astrophysical Journal*, 647, 128
- Erb, D. K., Steidel, C. C., Trainor, R. F., et al. 2014, *ApJ*, 795, 33
- Finkelstein, K. D., Finkelstein, S. L., Tilvi, V., et al. 2015, *The Astrophysical Journal*, 813, 78
- Furusawa, H., Kosugi, G., Akiyama, M., et al. 2008, *ApJs*, 176, 1
- Gawiser, E., Francke, H., Lai, K., et al. 2007, *ApJ*, 671, 278
- Giacconi, R., Rosati, P., & Tozzi, P. 2001, *The Astrophysical ...*, 551, 624
- Gordon, K. D., Clayton, G. C., Misselt, K. A., Landolt, A. U., & Wolff, M. J. 2003, *Apj*, 594, 279
- Gronwall, C., Ciardullo, R., Hickey, T., et al. 2007, *The Astrophysical Journal*, 667, 79
- Guaita, L., Gawiser, E., Padilla, N., et al. 2010, *The Astrophysical Journal*, 714, 255
- Guaita, L., Acquaviva, V., Padilla, N., et al. 2011, *The Astrophysical Journal*, 733, 114
- Gunn, J. E., & Stryker, L. L. 1983, *Statewide Agricultural Land Use Baseline 2015*, 52, 121
- Hagen, A., Ciardullo, R., Gronwall, C., et al. 2014, *The Astrophysical Journal*, 786, 59
- Hagen, A., Zeimann, G. R., Behrens, C., et al. 2016, *The Astrophysical Journal*, 817, 79
- Hagen, L. M. Z., Siegel, M. H., Hoversten, E. A., et al. 2017, *MNRA*, 466, 4540
- Hamana, T., Yamada, T., Ouchi, M., Iwata, I., & Kodama, T. 2006, 1938, 1929
- Harikane, Y., Ouchi, M., Ono, Y., et al. 2016, *The Astrophysical Journal*, 821, 123
- Harris, J., & Zaritsky, D. 2009, *The Astronomical Journal*, 138, 1243
- Hashimoto, T., Ouchi, M., Shimasaku, K., et al. 2013, *The Astrophysical Journal*, 765, 70
- Hashimoto, T., Verhamme, A., Ouchi, M., et al. 2015, *The Astrophysical Journal*, 812, 157

- Hashimoto, T., Ouchi, M., Shimasaku, K., et al. 2017, *MNRAS*, 465, 1543
- Hathi, N. P., Fevre, O. L., & Team, t. V. 2016, *A&A*, 588, A26
- Hayes, M., Östlin, G., Schaerer, D., et al. 2010, *Nature*, 464, 562
- . 2013, *The Astrophysical Journal*, 765, L27
- Hayes, M., Östlin, G., Duval, F., et al. 2014, *ApJ*, 782, 6
- Hildebrandt, H., Erben, T., Dietrich, J., et al. 2006, *A&A*, 452, 1121
- Hsieh, B. B.-C., Wang, W.-H. W., Yan, H., et al. 2012, *\Apjs*, 203, 23
- Hu, E. M., Cowie, L. L., Barger, A. J., et al. 2010, *The Astrophysical Journal*, 725, 394
- Ishikawa, S. 2017, PhD thesis, SOKENDAI (The Graduate University for Advanced Studies)
- Ishikawa, S., Kashikawa, N., Hamana, T., Toshikawa, J., & Onoue, M. 2016, *Monthly Notices of the Royal Astronomical Society*, 458, 747
- Kafle, P. R., Sharma, S., Lewis, G. F., & Bland-Hawthorn, J. 2014, *ApJ*, 794, 59
- Karman, W., Caputi, K. I., Caminha, G. B., et al. 2017, *A&A*, 599, A28
- Kashikawa, N., Shimasaku, K., Malkan, M. A., et al. 2006, *ApJ*, 2, 7
- Kashikawa, N., Shimasaku, K., Matsuda, Y., et al. 2011, *ApJ*, 734, 119
- Kashino, D., More, S., Silverman, J. D., et al. 2017, *arXiv*, 1703.08326, 1
- Kennicutt, R. C. 1998, *STAR FORMATION IN GALAXIES ALONG THE HUBBLE SEQUENCE*
- Khostovan, A. A., Sobral, D., Mobasher, B., et al. 2017, *arXiv*, 1705.01101
- Kojima, T., Ouchi, M., Nakajima, K., et al. 2017, *PASJ*, 69, 44
- Konno, A. 2014, *ApJ*, 797, 16
- Konno, A., Ouchi, M., Nakajima, K., et al. 2016, *The Astrophysical Journal*, 823, 20
- Kovač, K., Somerville, R. S., Rhoads, J. E., Malhotra, S., & Wang, J. 2007, *The Astrophysical Journal*, 668, 15
- Kroupa, P. 2001, *Monthly Notices of the Royal Astronomical Society*, 322, 231
- Kunth, D., Mas-Hesse, J. M., Terlevich, E., et al. 1998, *Astronomy and Astrophysics*, 334, 11
- Kusakabe, H., Shimasaku, K., Nakajima, K., & Ouchi, M. 2015, *The Astrophysical Journal*, 800, L29
- Lai, K., Huang, J.-s., Fazio, G., et al. 2008, *ApJ*, 674, 70
- Laigle, C., McCracken, H. J., Ilbert, O., et al. 2016, *The Astrophysical Journal Supplement Series*, 224, 1
- Landy, S. D., & Szalay, A. S. 1993, *The Astrophysical Journal*, 412, 64
- Lawrence, A., Warren, S. J., Almaini, O., et al. 2007, *Monthly Notices of the Royal Astronomical Society*, 379, 1599
- Lee, K., Giavalisco, M., Gnedin, O. Y., et al. 2006, *The Astrophysical Journal*, 642, 63
- Lin, L., Dickinson, M., Jian, H.-y., et al. 2012, *The Astrophysical Journal*, 756, 71
- Malhotra, S., & Rhoads, J. E. 2002, *ApJ*, 565, L71
- Mallery, R. P., Mobasher, B., Capak, P., et al. 2012, *ApJ*, 760, 128
- Matthee, J., Sobral, D., Oteo, I., et al. 2016, *Monthly Notices of the Royal Astronomical Society*, 458, 449
- McCracken, H. J., Milvang-Jensen, B., Dunlop, J., et al. 2012, *Astronomy & Astrophysics*, 544, A156
- Meurer, G. R., Heckman, T., & Calzetti, D. 1999, *ApJ*, 521, 64
- Moster, B. P., Naab, T., & White, S. D. M. 2013, *Monthly Notices of the Royal Astronomical Society*, 428, 3121
- Moster, B. P., Somerville, R. S., Newman, J. A., & Rix, H.-W. 2011, *The Astrophysical Journal*, 731, 113
- Moy, E., \mkbibboldBarmby, P., Rigopoulou, D., et al. 2003, *a&a*, 403, 493
- Murray, S., Power, C., & Robotham, A. 2013, *Astronomy and Computing*, 3, 23
- Nakajima, K., & Ouchi, M. 2014, *Monthly Notices of the Royal Astronomical Society*, 442, 900
- Nakajima, K., Ouchi, M., Shimasaku, K., et al. 2013, *The Astrophysical Journal*, 769, 3
- . 2012, *The Astrophysical Journal*, 745, 12
- Nestor, D. B., Shapley, A. E., Kornei, K. a., Steidel, C. C., & Siana, B. 2013, *The Astrophysical Journal*, 765, 47
- Nilsson, K. K., Tapken, C., Møller, P., et al. 2009, *A&A*, 498, 13
- Norberg, P., Baugh, C. M., Gaztañaga, E., & Croton, D. J. 2009, *Monthly Notices of the Royal Astronomical Society*, 396, 19
- Oke, J. B., & Gunn, J. E. 1983, *The Astrophysical Journal*, 266, 713
- Ono, Y., Shimasaku, K., Dunlop, J., et al. 2010a, *The Astrophysical Journal*, 724, 1524
- Ono, Y., Ouchi, M., Shimasaku, K., et al. 2010b, *Monthly Notices of the Royal Astronomical Society*, 402, 1580
- Östlin, G., Hayes, M., Duval, F., et al. 2014, *The Astrophysical Journal*, 797, 11
- Ota, K., Iye, M., Kashikawa, N., et al. 2008, *Apj*, 677, 12
- Oteo, I., Bongiovanni, A., Cepa, J., et al. 2012, *A&A*, 541, A65
- Ouchi, M., Shimasaku, K., Furusawa, H., et al. 2003, *The Astrophysical Journal*, 582, 60
- Ouchi, M., Shimasaku, K., Okamura, S., et al. 2004, *The Astrophysical Journal*, 611, 685
- Ouchi, M., Hamana, T., Shimasaku, K., et al. 2005, *The Astrophysical Journal*, 635, L117
- Ouchi, M., Shimasaku, K., Akiyama, M., et al. 2008, *The Astrophysical Journal Supplement Series*, 176, 301
- Ouchi, M., Shimasaku, K., Furusawa, H., et al. 2010, *The Astrophysical Journal*, 723, 869

- Ouchi, M., Harikane, Y., Shibuya, T., et al. 2017, arXiv, 00, 1704.07455v1
- Overzier, R. a., Heckman, T. M., Wang, J., et al. 2011, *The Astrophysical Journal*, 726, L7
- Pardy, S. A., Cannon, J. M., Sandberg, A., et al. 2014, *ApJ*, 101, 794
- Pei, Y. C. 1992, *Astrophysical Journal*, 395, 130
- Peñarrubia, J., Gómez, F. A., Besla, G., Erkal, D., & Ma, Y. Z. 2016, *Monthly Notices of the Royal Astronomical Society: Letters*, 456, L54
- Pentericci, L., Grazian, A., Scarlata, C., et al. 2010, *Astronomy and Astrophysics*, 514, A64
- Plank Collaboration. 2016, *A&A*, 594, 13
- Press, W. H., & Schechter, P. 1974, *The Astrophysical Journal*, 187, 425
- Rauch, M., Haehnelt, M., Bunker, A., et al. 2008, *The Astrophysical Journal*, 681, 856
- Reddy, N. a., Erb, D. K., Pettini, M., Steidel, C. C., & Shapley, A. E. 2010, *The Astrophysical Journal*, 712, 1070
- Reddy, N. A., Steidel, C. C., Pettini, M., et al. 2008, *The Astrophysical Journal Supplement Series*, 175, 48
- Reddy, N. A., Oesch, P. A., Bouwens, R. J., et al. 2017, arxiv, 1705.09302
- Rezaei Kh., S., Javadi, A., Khosroshahi, H., & Van Loon, J. T. 2014, *Monthly Notices of the Royal Astronomical Society*, 445, 2214
- Rodighiero, G., Daddi, E., Baronchelli, I., et al. 2011, *The Astrophysical Journal*, 739, L40
- Salpeter, E. E. 1955, *Astrophysical Journal*, 121, 161
- Sandberg, A., Guaita, L., Östlin, G., Hayes, M., & Kiaeerad, F. 2015, *A&A*, 580, A91
- Santini, P., Fontana, A., Castellano, M., et al. 2017, arXiv, 1706.07059
- Schlegel, D. J. D. J., Finkbeiner, D. P. D. P., & Davis, M. 1998, *The Astrophysical Journal*, 500, 525
- Scoville, N., Abraham, R. G., Aussel, H., et al. 2007, *ApJs*, 172, 38
- Shapley, A. E., Steidel, C. C., Pettini, M., & Adelberger, K. L. 2003, *The Astrophysical Journal*, 588, 65
- Shibuya, T., Ouchi, M., Nakajima, K., et al. 2014, *The Astrophysical Journal*, 788, 74
- Shibuya, T., Ouchi, M., Harikane, Y., et al. 2017a, arXiv, 1704.08140, doi:10.1093/pasj/xxx000
- . 2017b, arXiv, 00, 1
- Shimakawa, R., Kodama, T., Shibuya, T., et al. 2017, *MNRAS*, 468, 1123
- Shimasaku, K., Kashikawa, N., Doi, M., et al. 2006, *Publications of the Astronomical Society of Japan*, 58, 313
- Shioya, Y., Taniguchi, Y., Sasaki, S. S., et al. 2009, *The Astrophysical Journal*, 696, 546
- Shivaei, I., Reddy, N., Shapley, A., et al. 2017, *The Astrophysical Journal*, 837, 157
- Simon, P. 2007, *Astronomy*, 714, 711
- Skelton, R. E., Whitaker, K. E., Momcheva, I. G., et al. 2014, *The Astrophysical Journal Supplement Series*, 214, 24
- Sobral, D., Best, P. N., Geach, J. E., et al. 2010, *Monthly Notices of the Royal Astronomical Society*, 404, 1551
- Taniguchi, Y., Ajiki, M., Nagao, T., et al. 2005, *Publications of the Astronomical Society of Japan*, 57, 165
- Taniguchi, Y., Scoville, N., Murayama, T., et al. 2007, *The Astrophysical Journal Supplement Series*, 172, 9
- Taylor, E. N., Franx, M., van Dokkum, P. G., et al. 2009, *The Astrophysical Journal Supplement Series*, 183, 295
- The Astropy Collaboration, Robitaille, T. P., Tollerud, E. J., et al. 2013, *Astronomy & Astrophysics*, 558, A33
- Tinker, J. L., Robertson, B. E., Kravtsov, A. V., et al. 2010, *The Astrophysical Journal*, 724, 878
- Tomczak, A., Quadri, R., & Tran, K. 2013, *ApJ*, 783, 85
- Tomczak, A. R., Quadri, R. F., Tran, K.-V. H., et al. 2016, *The Astrophysical Journal*, 817, 118
- Totsuji, H., & Kihara, T. 1969, *Publications of the Astronomical Society of Japan*, 21, 221
- van der Marel, R. P., Alves, D. R., Hardy, E., Suntzeff, N. B., & Al, V. A. N. D. E. R. M. E. T. 2002, *ApJ*, 124, 2639
- van der Marel, R. P., & Kallivayalil, N. 2014, *The Astrophysical Journal*, 781, 121
- Vanzella, E., Giavalisco, M., Dickinson, M., et al. 2009, *The Astrophysical Journal*, 695, 1163
- Vargas, C. J., Bish, H., Acquaviva, V., et al. 2014, *The Astrophysical Journal*, 783, 26
- Verhamme, A., Schaerer, D., & Maselli, A. 2006, *A&A*, 460, 397
- Wang, W., Cowie, L. L., Barger, A. J., Keenan, R. C., & Ting, H. 2010, *The Astrophysical Journal Supplement*, 187, 251
- Wang, W., Han, J., Cooper, A. P., et al. 2015, *Monthly Notices of the Royal Astronomical Society*, 453, 377
- Weisz, D. R., Dolphin, A. E., Skillman, E. D., et al. 2013, *Monthly Notices of the Royal Astronomical Society*, 431, 364
- Whitaker, K. E., Franx, M., Leja, J., et al. 2014, *ApJ*, 795, 104
- Wilkinson, M. I., & Evans, N. W. 1999, *Monthly Notices of the Royal Astronomical Society*, 310, 645
- Yagi, M., Suzuki, N., Yamanoi, H., et al. 2013, *PASJ*, 65, 22
- Yamada, T., Nakamura, Y., Matsuda, Y., et al. 2012, *ApJ*, 79, 143
- Zehavi, I., Weinberg, D. H., Zheng, Z., et al. 2004, *The Astrophysical Journal*, 608, 16